ELSEVIER

Contents lists available at ScienceDirect

# **Applied Thermal Engineering**

journal homepage: www.elsevier.com/locate/ate



# Research paper

# Heat release behavior in a natural gas lean-burn SI marine engine: Exploring the impact of bowl-in and squish combustion on performance and emissions

Konstantinos I. Kiouranakis <sup>a, \*</sup>, Peter de Vos <sup>a</sup>, Robbert Willems <sup>b, \*</sup>, Harsh Darshan Sapra <sup>c</sup>, Rinze Geertsma <sup>a, d</sup>

- <sup>a</sup> Faculty of Mechanical Engineering, Delft University of Technology, Mekelweg 2, Delft, 2628 CD, The Netherlands
- b Powertrains Department, Netherlands Organisation for Applied Scientific Research (TNO), Helmond, The Netherlands
- <sup>c</sup> Department of Automotive Engineering, Clemson University, SC, USA
- <sup>d</sup> Faculty of Military Sciences, Netherlands Defence Academy, Den Helder, The Netherlands

#### ARTICLE INFO

#### Keywords: Internal combustion engine Spark ignition Heavy-duty Two-stage combustion Natural gas

#### ABSTRACT

Emerging clean fuels with high octane rating make spark ignition (SI) technology a promising candidate for heavy-duty applications. The conversion of existing diesel engines to SI operation can accelerate the adoption of these fuels. This study investigates the combustion characteristics of a 500 kWe marine lean-burn (LB) homogeneous charge SI engine with a flat cylinder head and a hemispherical bowl-in piston. It focuses on the relationship between fuel distribution and phasing across the distinct bowl-in and squish combustion phases and their impact on efficiency and emissions in multicylinder engines. The effects of air excess ratio, spark timing, and intake air temperature are systematically assessed. Dedicated measurements of methane and total unburned hydrocarbon emissions enable a comprehensive evaluation of combustion performance and emissions. Results confirm the presence of a slower squish phase, differing from conventional SI engines, and highlight the influence of the squish region's surface-to-volume ratio on flame propagation. The sensitivity of combustion behavior to control parameters such as air excess ratio and ignition timing is demonstrated, with notable differences: while richer mixtures advance bowl-in and squish phases, earlier ignition timing delays the squish phase. Despite this, both mixture enrichment and ignition timing advancement improved performance, increasing brake thermal efficiency by 25% and 10%, respectively. Methane emissions remained within typical ranges for marine SI engines and NO<sub>v</sub> emissions met Tier III limits at nominal conditions; yet the persistent challenge of methane slip underscores the need for more comprehensive regulatory standards addressing both CH<sub>4</sub> and NO<sub>x</sub> emissions.

# 1. Introduction

Diesel engines remain the dominant power source for heavy-duty (HD) and marine transportation due to their operational robustness and efficiency [1], with spark ignition (SI) engine technology traditionally used in light-duty (LD) automotive applications [2]. SI engines can be particularly well-suited for emerging alternative fuels, such as ammonia [3], methanol [4], and hydrogen [5], due to the autoignition challenges of these fuels with compression ignition (CI) engines. Nevertheless, the maritime sector has largely focused on dual-fuel (DF) strategies for using alternative fuels, particularly natural gas (NG) in recent years, retaining diesel combustion principles [6,7]. Although this approach is effective, it still relies on a high reactive fuel like diesel for ignition, which reliance in many cases is still significant, limiting the upscale and full transition to alternative fuels [8].

A promising alternative involves converting existing diesel engines to SI operation with minimal modifications by replacing the fuel injector with a spark plug and incorporating a low-pressure fuel injection system into the intake path [9,10]. This approach is relatively straightforward, requiring no major engine redesign, and could be particularly suitable for compact marine engines where limited cylinder head space poses challenges for pre-chamber integration [11]. Additionally, this strategy often includes modifying the piston crown to slightly lower the compression ratio (CR) and optimize the in-cylinder flow regime for flame propagation rather than spray combustion [9]. Unlike conventional SI engines, which aim to minimize heat losses by reducing combustion chamber surface areas, this conversion approach leverages an enhanced flow regime that supports faster combustion and enables leaner mixture operation. In contrast to pre-chamber-based SI technology, this concept relies on a relatively well-homogenized charge

E-mail address: K.I.Kiouranakis@tudelft.nl (K.I. Kiouranakis).

<sup>\*</sup> Corresponding author.

# Abbreviations

aTDC After Top Dead Center
bTDC Before Top Dead Center
BTE Brake Thermal Efficiency

CA Crank Angle

CAD Crank Angle Duration CA50 **Combustion Phasing** CD Combustion Duration CI Compression Ignition  $CO_2$ Carbon Dioxide COV Coefficient of Variance CR Compression Ratio DAS Data Acquisition System

DF Dual-Fuel

DoE Design-of-Experiment EVO Exhaust Valve Open

HD Heavy-Duty HRR Heat Release Rate

ICE Internal Combustion Engine

ID Ignition Delay

IMEP Indicated Mean Effective Pressure IMO International Maritime Organization

IVC Inlet Valve Closing
IVO Inlet Valve Opening

LB Lean-Burn

LBSI Lean-Burn Spark Ignition

LD Light-Duty

MEP Mean Effective Pressure

NG Natural Gas

NO<sub>x</sub> Nitrogen Oxide

ON Octane Number

Pmax Peak Pressure

PRR Pressure Release Rate

SI Spark Ignition
ST Spark Timing
TDC Top Dead Center

TKE Turbulent Kinetic Energy UHC Unburned Hydrocarbon

through the combustion chamber [12]. Notably, pre-chamber designs have not yet been applied to smaller marine engines, as evidenced by prior research [13–15].

Retaining a diesel-like combustion chamber and swirl-inducing inlet ports [16], as implemented in the patented nebula combustion system [11,17], provides optimum conditions for ignition and fast burning by the 'swirl killing' phenomenon as the piston approaches top dead center (TDC) [11]. This phenomenon, combined with enhanced tumble flow in bowl-in pistons, leads to greater turbulence levels in the combustion chamber [18,19]. The greater turbulence subsequently enhances flame stability and significantly increases the potential of these engines to run on lean mixtures, thereby extending their capacity to reduce certain emissions and improve fuel economy [20]. Additionally, alternative fuels like NG and methanol, which have wider flammability ranges, can further improve the lean-burn capabilities of these engines [21,22]. This makes this technology very promising to meet environmental targets without the need for extra exhaust treatment systems such as three-way catalysts in conventional stoichiometrically operated SI engines [20,23] or selective catalytic reduction technology in marine DF engines [24,25]. Improving lean-burn capabilities in SI

engines reduces  $NO_x$  by lowering combustion temperatures, while it also decreases CO and unburned hydrocarbon (UHC) emissions thanks to the greater oxygen availability [26,27]. Further, the extension of dilution limits, combined with the high octane rating of alternative marine fuels, allows these lean-burn (LB) SI concepts to extend their knock limits [28]. This enables them to operate at higher CRs and efficiencies than their conventional SI counterparts [29,30].

In addition to inducing high turbulence, the squish regions in such chamber geometries can result in distinct combustion behavior, characterized by two combustion stages: a first rapid combustion phase within the bowl and a slower combustion phase in the squish region, unlike conventional SI combustion [19,31] with flat piston geometries and single-phase combustion modes. Note that, despite the apparent high turbulence, this engine concept is highly sensitive to combustion phasing due to the existence of the second later combustion stage [32]. The fuel distribution across the two combustion stages influences the combustion stability and overall performance of the engine [33]. For instance, the typical effect of advancing ignition timing in the combustion phasing on efficiency and emissions can differ from that of conventional engines [34]. Advanced spark timing typically deteriorates combustion and emissions performance in this engine type due to unfavorable conditions for the second squish combustion phase [35,36]. A rise in the amount of fuel combusting in this phase can therefore overturn the benefit of the fast first combustion stage and result in reduced overall efficiency, leading to elevated UHC emissions [37]. Further, the combination of higher turbulence and prolonged combustion promote heat transfer processes in the cylinder and can therefore deteriorate engine efficiency even further.

Recent research on LBSI strategies for heavy-duty and marine engines has predominantly focused on advanced pre-chamber stratification concepts, both in fundamental studies [38-40] and in the development of commercial marine SI products [14,15,41,42]. As a result, the optimization potential and practical advantages of homogeneous, open-chamber LBSI concepts — especially suitable for retrofitting diesel engines — have received comparatively little attention. This gap is particularly significant for marine-scale, multi-cylinder engines, which engines could play a key role in the energy transition. While singlecylinder experimental setups and numerical studies have provided valuable insights into alternative fuels [22,43,44], combustion chamber designs and operating strategies [45-48], there remains a lack of experimental data on multi-cylinder engines that can capture overall performance, and the relationships between efficiency and emissions with the inter-cylinder combustion dynamics. Specifically, few studies have explored the interplay between distinct combustion phases and emissions - particularly methane and total UHC - which are of growing environmental concern. Methane slip, in particular, is now recognized as a critical challenge for marine gas engines [49,50], but available data for large-scale SI concepts remain limited [50].

This study addresses these gaps by providing new, multi-cylinder experimental data and phase-resolved combustion analysis from a 500 kWe NG LBSI marine engine featuring diesel-based geometry with a flat cylinder head and a hemispherical bowl-in piston. This research examines the relationship between distinct combustion phases — bowlin and squish — and both efficiency and emissions, including methane, to better understand the fundamentals of this process in larger-scale multicylinder engines. The influence of key parameters — air excess ratio, spark timing, and intake air temperature - on combustion stages, efficiency, and emissions is systematically explored. The main objective of this study is to provide deeper insights into the combustion and emissions performance of the diesel-adaptable LBSI concept for marine applications and to explore potential optimization strategies. Ultimately, these findings can support the marine sector's transition from petroleum-based fuels towards less carbon-intensive alternatives, such as methanol or ammonia, by focusing on the research and development of such dedicated engine conversion strategies for emerging sustainable fuels.

Table 1
Engine specifications.

Engine type	8-cylinder, turbocharged,
	lean-burn, 4-stroke
Ignition mode	Spark Ignition
Combustion chamber	Flat head and bowl-in piston
Bore × Stroke [mm]	170 × 190
Displacement [L]	34.5
Rated power/speed [kWe/rpm]	500/1500
Compression Ratio [-]	12:1
Number of valves [-]	4
Intake valve opens/closes [°CA aTDC]	337/-122
Exhaust valve opens/closes [°CA aTDC]	140/377

#### 2. Experimental setup

The experimental setup, as illustrated in Fig. 1, uses an 8-cylinder, four-stroke, turbocharged, marine high-speed NG LBSI engine. The engine is rated at 500 kWe at 1500 rpm and features a minimal valve overlap, with the specifications of the test engine given in Table 1. The engine, originally designed as a diesel engine, was converted into gas-powered with minimal modifications to facilitate its transition to SI operation. As part of this conversion, the piston geometry was redesigned with a new bowl-in piston, reducing the compression ratio to 12:1. The design aimed to harness squish flow to enhance turbulence within the cylinder near TDC, promoting faster flame propagation and improving lean-burn combustion capabilities, while retaining the core architecture of the original diesel design. The hemispherical bowl-in piston crown is shown in Fig. 2, with the intended squish-to-tumble flow transition illustrated in Fig. 3.

#### 2.1. Data acquisition system

The data acquisition system (DAS) in the engine setup typically comprises two main components: one for in-cylinder measurements using a Kistler Type 2893 A Kibox and another for external cylinder data collection, including emissions measurements by a HORIBA PG-350 analyzer. All cylinders are equipped with uncooled Kistler 7061C piezoelectric pressure sensors, connected to a Kistler 5064C charge amplifier. Additionally, an optical crank angle encoder with 720 marks is used to measure the crankshaft angle, enabling pressure data collection with a resolution of 0.5 °CA. While this engine has been previously used in studies [51,52], new pressure sensors were mounted in a minimal and controlled recessed fashion on the periphery of all cylinder heads, as shown in Fig. 4. After installing the new sensors, several offline evaluation techniques were used to verify the accuracy of the updated measurement setup [53,54]. Fig. 4 demonstrates a detailed scheme with the experimental apparatus in the engine lab. For this study, an additional flame ionization detector, a Thermo-FID PT84 analyzer, was used to capture methane and total UHC emissions. NG is injected upstream of the compressor, with its flow rate being monitored by a Bronkhorst F-106Cl gas flow meter. It should be noted that the NG used in this study is characterized as a low calorific value gas due to the high amount of nitrogen it contains, with its composition and properties summarized in Table 2. The main instruments of the DAS are given in Table 3.

# 2.2. Operating test method and conditions

The primary aim of this research is to examine the steady-state operation of this NG LBSI engine. To ensure stability during testing, the engine was operated for at least five minutes between the operating points' transitions, with a continuous monitoring of parameters such as exhaust temperature, fuel flow, and emissions to ensure steady-state conditions. This experimental study builds on a previous one conducted with the same engine setup [55], which focused on the combustion



Fig. 1. The marine four-stroke spark ignition engine in the lab.

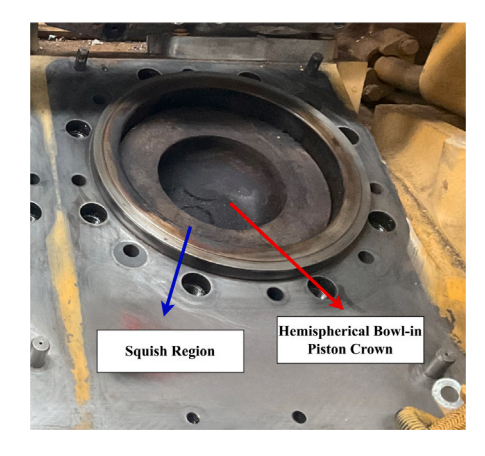
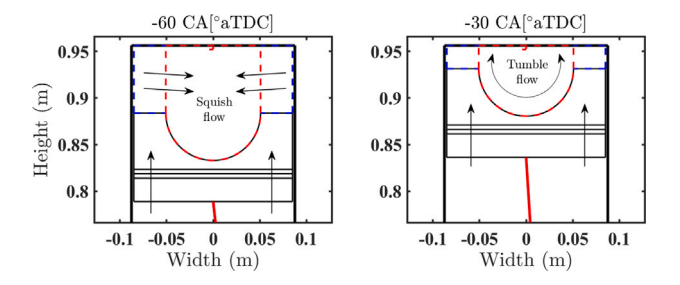


Fig. 2. Piston crown.



 $\textbf{Fig. 3.} \ \ \textbf{Squish to tumble flow transition during compression approaching TDC.}$ 

stability and identification of different stability regions. Key differences in the new dataset include: (1) an increased number of operating points tested, (2) the addition of intake air temperature sweeps, and (3) the use of the FID analyzer for a better quantification of combustion efficiency, methane and total UHC emissions.

Consequently, this study advances the referenced previous works on the same engine by integrating upgraded pressure sensors and a comprehensively validated DAS. The data processing methodology has been refined to ensure greater consistency in combustion diagnostics. Dedicated methane and total UHC emissions measurements were conducted for the first time for this setup, linking emissions directly to combustion performance. Moreover, recent optical access insights inform a phase-resolved analysis of combustion behavior, distinguishing the combustion diagnostic analysis of this work.

The current experimental study involved 26 operating points, including load, air excess ratio ( $\lambda$ ), spark timing (ST) and intake air temperature sweeps. The load levels for the sweeps were kept consistent with the preceding study under the same justification of this

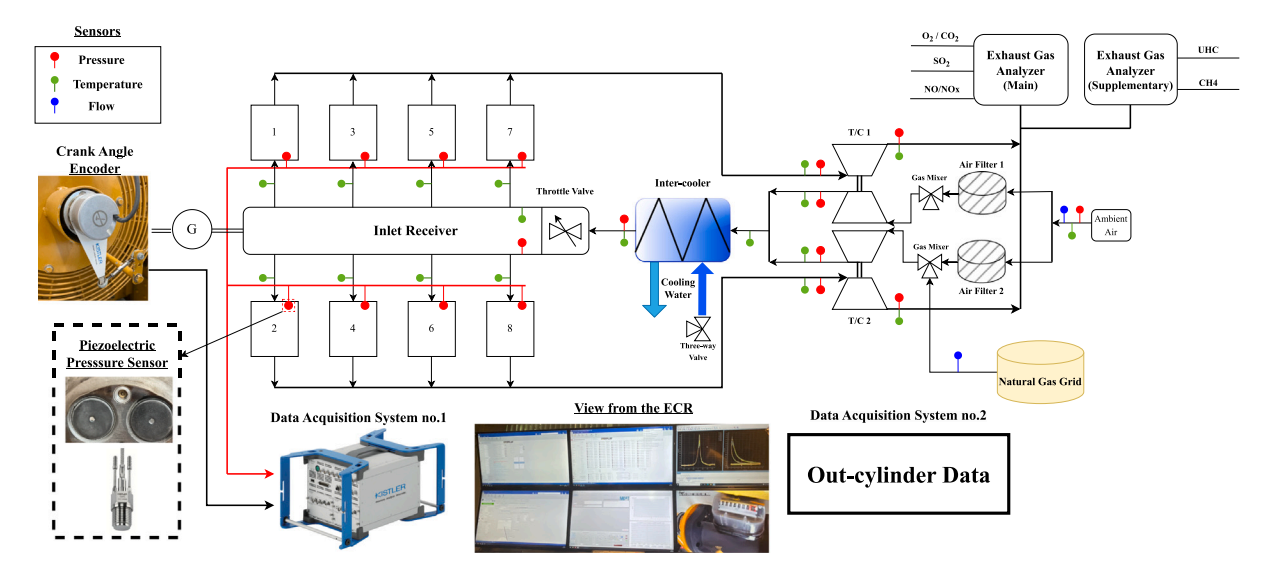


Fig. 4. Schematic diagram of the experimental apparatus.

Table 2
Main constituents in the NG and properties

80.8
3.18
0.71
13.1
1.69
0.77
38.12
39.94
83

Table 3

Main measurement instruments of the DAS.

Instrument	Sensor type	Unit	Accuracy
Exhaust pressure	JUMO dTRANS p30	bar	±0.5%FS
Natural gas flow meter	Bronkhorst F-106Cl	m <sup>3</sup> /h	$\pm 1\%FS$
Cylinder pressure	Kistler 7061C non-cooled	bar	$\pm 0.5\%FS$
Exhaust gas analyzer	Horiba PG-350	ppm	$\pm 2\%FS$
Exhaust gas analyzer	Thermo-FID PT84/LT	mg/m <sup>3</sup>	±4%FS
Intake-Exhaust temperature	K-type thermocouple	K	±0.4%FS

study and to facilitate meaningful comparisons if required. Pressure traces were recorded for the top in-line cylinders 1, 3, 5, and 7 over 400 consecutive cycles at each operating point. The engine is supplied with NG from the local low-pressure gas grid. During this experimental campaign, the insufficient NG grid pressure restricted the maximum achievable load to 432 kWe. Table 4 illustrates the engine test conditions during this experimental study.

# 3. Data-analysis methodology

This section provides details regarding the followed methodology for analyzing the data from the measurement campaign in this engine. All the used models for the pressure-based performance and combustion diagnostic analysis are developed in the environment of MATLAB and Simulink [56]. As the primary focus of the study lies in the combustion diagnostics of the engine, there is a high need for accurate and representative pressure traces for each operating condition.

# 3.1. In-cylinder pressure data

For the referencing of pressure traces, the two-point polytropic compression pegging method is used, implemented automatically for each

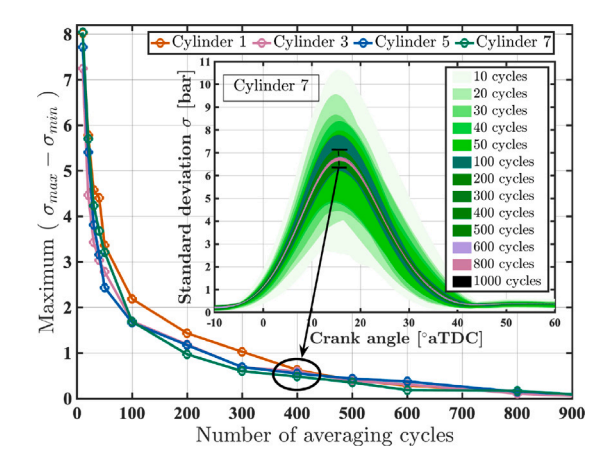


Fig. 5. Standard deviation with different number of average cycles.

cycle by the Kibox. The pegging points were set at 65° and 100 °CA bTDC, using 1.33 for the value of the polytropic coefficient [57]. An offline verification has also taken place to ensure the correct pegging of pressure traces [58]. The thermodynamic loss angle was determined using the model developed and validated by Sta s' [59], and further validated from the analysis of Tazerout et al. [60].

Given that heat release analysis is based on an ensemble-averaged pressure trace, determining the optimal number of cycles to average is essential, as this value largely depends on the specific engine characteristics [61]. This study applied the method proposed by Maurya [62] to establish the optimal number of cycles for pressure averaging, to ensure robust heat release analysis at each operating condition. An additional measurement campaign involving numerous consecutive cycles at several operating conditions indicated that averaging over 400 cycles can provide a suitable balance between data processing efficiency and accuracy. Fig. 5 shows the maximum standard deviation observed of one operating condition for different averaging number across all cylinders. This deviation on the y-axis represents the maximum difference between the minimum and maximum standard deviation in the envelope during combustion, as illustrated in the sub-figure within Fig. 5. A subplot in the figure demonstrates the variation in the pressure envelope when using a different number of averaged cycles for cylinder 7. All cylinders exhibit a maximum standard deviation below 1 bar, with 400 as the averaging number.

Table 4

Sweep	Case	Gen. Power [kWe]	Fuel flow [m <sup>3</sup> /h]	Air excess ratio [-]	MAP [bar]	MAT [K]	ST [°bTDC]
	1	101	55.23	1.43	0.703	312.6	20
	2	200	83.82	1.57	1.118	312.0	20
Load	3	300	111.16	1.60	1.483	311.4	20
	4	400	138.99	1.58	1.858	310.4	20
	5	432	148.24	1.57	1.989	310.2	20
	6	201	79.96	1.25	0.911	311.3	20
	7	200	80.11	1.38	0.979	314.7	20
	8	200	80.97	1.45	1.025	312.1	20
Air excess ratio	9	200	81.92	1.50	1.060	312.3	20
Air excess ratio	10	200	85.16	1.59	1.155	311.8	20
	11	200	89.70	1.65	1.254	312.3	20
	12	200	96.44	1.71	1.376	313.4	20
	13	200	100.26	1.77	1.430	311.6	20
	14	200	79.30	1.53	1.048	312.0	26
	15	200	80.33	1.54	1.071	314.6	24
Spark timing	16	200	81.49	1.54	1.085	314.2	22
spark tilling	17	200	83.44	1.53	1.102	312.2	19
	18	200	84.77	1.53	1.121	312.5	18
	19	200	86.24	1.53	1.145	313.8	17
	20	200	84.45	1.60	1.193	335.9	20
	21	200	83.68	1.57	1.159	330.8	20
	22	200	83.49	1.56	1.146	327.0	20
Intake temperature	23	200	83.09	1.55	1.122	320.6	20
	24	200	82.88	1.53	1.101	314.6	20
	25	200	82.39	1.51	1.074	308.2	20
	26	200	82.26	1.50	1.064	305.4	20

Additionally, the estimated values of key parameters, such as air excess ratio, emissions metrics, and heat release characteristics, are crucial for both diagnostic analysis and subsequent modeling studies, including computational fluid dynamics simulations. To ensure reliability in these parameters up to a certain confidence interval, this research adopts the uncertainty quantification methodology proposed by Gainey et al. [63] over the uncertainties of the measured parameters. The conservative approach using the mean cyclic uncertainty is applied to estimate the final uncertainty in ensemble-averaged values.

#### 3.2. Performance and emissions

After encountering some difficulties with the measurements of the air flow sensor that is a part of the measuring equipment of the engine setup, air flow, together with air-to-fuel ratios and  $\lambda$ , is estimated based on the oxygen concentration of the exhaust gases. The combustion efficiency is estimated from the unused energy of the fuel constituents in the exhaust gases, using Eq. (1).

$$n_{\rm c} = (1 - \frac{1 + \lambda \cdot \text{AFR}_{\text{stoich.}} \cdot \sum_{i=1}^{n_{\rm UHC}} y_i \cdot Q_{\rm HV,i}}{\text{LHV}_{\text{fuel}}}) \cdot 100\% \tag{1}$$

where  $\lambda$  is the air excess ratio, AFR<sub>stoich</sub> is the stoichiometric air-to-fuel ratio for the NG, with  $y_i$  and  $Q_{HV_i}$  being the mass fraction and lower heating value of the corresponding species in the exhaust.

To analyze the efficiency of the engine and better analyze the fuel energy components, this study uses the relative engine performance measure of mean effective pressure (MEP) to quantify the key energy balance components (EBCs) [34], using Eq. (2).

$$MEP_{EBC_i} = \frac{EBC_i}{V_{displacement}}$$
 (2)

where  $V_{\text{displacement}}$  is the displaced cylinder volume and  $EBC_i$  is the individual energy component. These components will be used to analyze the energy share paths deriving from the fuel energy and presented in the Sankey diagram of Fig. 9. Fuel slip energy or combustion losses are calculated based on the fuel energy input and combustion efficiency, while heat transfer is determined from the calibrated heat transfer model at EVO, which is also used for the estimation of the gross heat release rate (gHRR). Gross indicated mean effective pressure (IMEP), as

well as pump and net MEPs, are computed directly from the cylinder pressure traces. Brake MEP is estimated using the measured generated electric power and the know generator efficiency. Exhaust and friction losses are then quantified by closing the energy balance for gHRR and net IMEP, respectively. The resulting MEPs are used to determine the fuel's energy share paths in the figures presented in Section 4.

Brake thermal efficiency (BTE) is calculated based on the measured generator power ( $P_{\text{generator}}$ ) in kWe, the generator efficiency  $n_{\text{generator}}$ and the mass consumption rates of NG ( $\dot{m}_{\rm NG}$ ) in kg/s, using Eq. (3).

$$BTE = \frac{P_{\text{generator}}}{n_{\text{generator}} \cdot \dot{m}_{\text{NG}} \cdot \text{LHV}_{\text{NG}}} \cdot 100\%$$
 (3)

Regarding emissions, this study normalizes the concentration of measured gaseous emissions, including NO<sub>x</sub>, CO, CH<sub>4</sub> and total UHC, in the exhaust gases in flow rates of the corresponding pollutant per unit brake power output, using Eq. (4). Specific NO<sub>v</sub> emissions are calculated as the total weighted NO<sub>2</sub> in accordance with IMO standards [64].

$$Emission_{\text{specific}} = \frac{\dot{m}_{\text{emission}}}{P_{\text{brake}}} \tag{4}$$

Cycle-to-cycle variations are analyzed through the coefficient of variation (COV) for IMEP, defined by Eq. (5), with the mean value and standard deviation being given by Eqs. (6) and (7), respectively.

$$COV_x = \frac{\sigma_x}{\mu_x} \cdot 100\% \tag{5}$$

$$\mu_{x} = \frac{\sum_{i=1}^{N_{\text{cycles}}} x_{i}}{N_{\text{cycles}}} \tag{6}$$

$$\mu_{x} = \frac{\sum_{i=1}^{N_{\text{cycles}}} x_{i}}{N_{\text{cycles}}}$$

$$\sigma_{x} = \sqrt{\frac{\sum_{i=1}^{N_{\text{cycles}}} (x_{i} - \mu_{x})^{2}}{N_{\text{cycles}}}}$$
(6)

Based on the previous study on this engine setup [55] and other similar studies [11], COV<sub>IMEP</sub> appears a good representative parameter for evaluating combustion stability over other parameters like peak pressure, with 3% being a reasonable limit for acceptable stability in these engines to maintain adequate efficiency levels.

#### 3.3. Heat release analysis

The used heat release model is a zero-dimensional, single-zone thermodynamic model based on the first law of thermodynamics for a closed system during the non-flow period (inlet valve closing (IVC) to exhaust valve opening (EVO)) [34]. An example of its calculations is Eq. (8) that calculates the gHRR, with both crevice and blow-by losses being neglected [65].

$${\rm gHRR} = {\rm aHRR} + \dot{Q}_{\rm loss} = m \cdot c_{\rm v}(\theta) \cdot \frac{dT(\theta)}{d\theta} + p(\theta) \cdot \frac{dV(\theta)}{d\theta} + \dot{Q}_{\rm loss} \tag{8}$$

where aHRR is the apparent HRR, m is the trapped in-cylinder mass,  $c_v$  is the mixture's specific heat at constant volume, T is the estimated bulk gas temperature calculated by the ideal gas law, p is the measured in-cylinder pressure, V is the measured in-cylinder volume,  $\theta$  the crank angle degree, and  $Q_{\rm loss}$  is the estimated heat transfer rate through the cylinder boundaries.

The heat release model assumes perfect homogeneity of the gases in the combustion chamber, with air, fuel and stoichiometric gases as constituents. The single point injection of natural gas (upstream of the compressor) and its gaseous state, combined with the engine speed (1500 rpm), ensure ample mixing time for fuel and air [66]. This minimizes local mixture variations, allowing the effects of control parameters like air excess ratio and spark timing to be interpreted in the context of a well-mixed charge. Stoichiometric gases are modeled as the products from stoichiometric combustion of the fuel. To estimate trapped conditions at IVC position, the residual gas (RG), i.e., the internal exhaust gas recirculated, mass is first estimated using the ideal gas law at the inlet valve opening (IVO) condition, with its temperature approximated as the measured exhaust outlet temperature [34,67]. The temperature at IVC is then calculated based on the mixing between the inducted and RG masses, with the temperature of the inducted mass being estimated from the measured temperature at the intake runner, considering heat pickup from the intake valves and ports.

The thermodynamic properties of the species, including specific heat ratios and enthalpies, are calculated based on the in-cylinder gas dynamic composition and temperature via power series [68]. The pressure signal used for each operating condition was derived from the ensemble-average for 400 consecutive cycles across all in-line cylinders, minimizing errors related to variation in gas path dynamics in multicylinder configurations. Heat transfer was modeled using the Woschni correlation using Eq. (9) to estimate the convective heat transfer coefficient  $h_{\rm woschni}$  [69], and total heat loss deriving from Eq. (10). Since heat transfer depends on specific engine and operation conditions, the estimated combustion efficiency at each operating point was used to calibrate the heat loss model [70]. After estimating the gHRR, the cumulative mass fraction burnt is calculated using Eq. (11).

$$h_{\text{woschni}} = C_0 \cdot \frac{1}{D_b^{0.214}} \frac{p^{0.786}}{T^{0.525}} \cdot [(2.28 + 0.308 \cdot \text{SR}) \cdot c_m + 0.00324 \cdot \frac{p - p_0}{p_1} \frac{V_S}{V_1} \cdot T_1]$$
(9)

where  $C_0$  is the calibrating parameter,  $D_b$  is the bore diameter, SR is the swirl ratio,  $c_m$  is the mean piston speed,  $p_0$  is the motoring pressure,  $V_S$  the stroke volume, and  $p_1$ ,  $V_1$ , and  $T_1$  are the pressure volume and temperature at IVC, respectively.

$$\dot{Q}_{\rm loss} = A_{\rm wall} \cdot h_{\rm woschni} \cdot (T - T_{\rm wall}) \tag{10}$$

where  $A_{\rm wall}$  and  $T_{\rm wall}$  are the surface are and temperature of the wall, respectively.

$$MFB = \frac{\int_{\text{ST}}^{\text{EVO}} \frac{\text{gHRR}}{\text{LHV}(\theta)} d\theta}{m_{\text{fuel, trapped}}}$$
 (11)

where LHV's temperature dependence is considered. The crank angle corresponding to x% of MFB, referred to as CAx, was determined to characterize different combustion phases.

The distinct combustion behavior of this engine strategy, combined with the study's focus on understanding the influence of combustion phasing on engine performance, necessitates a well-defined methodology for characterizing combustion phasing. Fig. 6 illustrates the

implemented combustion staging framework, highlighting the defined combustion phases through various curves, including the aHRR profile and the in-cylinder pressure signal. While conventional SI engines typically employ CA05 or CA10 to quantify ignition lag or kernel development phase, recent studies suggest CA01 may be more accurate for representing the start of combustion [10,35]. Nevertheless, given the inherent uncertainties in early combustion detection, this study will adhere to CA10 as the threshold to marking the flame development phase end, thereby the start of the bowl-in stage. CA10 is selected over CA05 for two main reasons: (1) CA10 is widely used as the indicator for the start of the combustion in conventional SI engines, which aligns with the start of the main bowl-in combustion phase in this LBSI concept; and (2) CA10 is less sensitive to aHRR signal noise and better centered with the first inflection point in the aHRR profile (see Fig. 22 in Appendix A), which could be alternatively used as the indicator for start of combustion.

The transitional point between bowl-in and squish combustion phases follows the established methodology of Liu et al. [35] indicated by the second inflection point in the aHRR profile in Fig. 6c, i.e., root of the second derivative of the aHRR curve. The use of the second aHRR inflection point to denote combustion phasing transition is based on correlations established in prior optical diagnostic studies of similar chamber geometries. While this approach provides a practical framework for phase identification in such engine strategies, the absence of in-cylinder visualization in the current testbed limits the correct establishment of such transition points and represents an approximation due to potential overlap between combustion stages.

CA95 is finally used to identify the end of the squish combustion phase. Three distinct combustion phases are consequently defined:

- Phase I (Flame development): Spanning from ST to CA10, including ignition lag.
- Phase II (Bowl-in combustion): Extending from CA10 to the second aHRR inflection point, characterizing the rapid flame propagation stage within the bowl region.
- 3. **Phase III (Squish combustion):** Covering the interval from Phase II conclusion to CA95, defining the slower flame propagation within the squish region.

Combustion duration (CD) is, therefore, quantified as the interval CA10-CA95. It should be noted that the MFB obtained using this methodology is correlated with the cumulated aHRR rather than the gHRR to avoid uncertainties associated with the heat transfer model.

# 4. Results and discussions

#### 4.1. Combustion characteristics

There were no indications of knock at any of the operating points tested during this experimental campaign. The primary challenge for these LBSI concepts remains combustion stability [44]. The lean capabilities of this engine technology also highlight its potential over conventional SI to utilize high specific heats in the chamber to improve efficiency closer to that of diesel engines.

Fig. 7 illustrates the cycle-by-cycle variation (CCV) of both inpressure and heat release across all cylinders for Case 2. It also includes the variation for the mean cylinder, as discussed in Section 3.3. All individual cylinders demonstrate good and relatively similar combustion stability, with COV values lower than 3%. It is evident that a number of individual cycles show delayed combustion phasing, which is expected in this type of LBSI engines. However, none of the average heat release profiles across the cylinders display such a distinct late combustion phase, with all average profiles coinciding well, indicating consistent combustion phasing across the cylinders. Cylinder 7, which experiences the fewest late-burning individual cycles, exhibits the highest work output and the lowest COV. Although the reduced occurrence of late

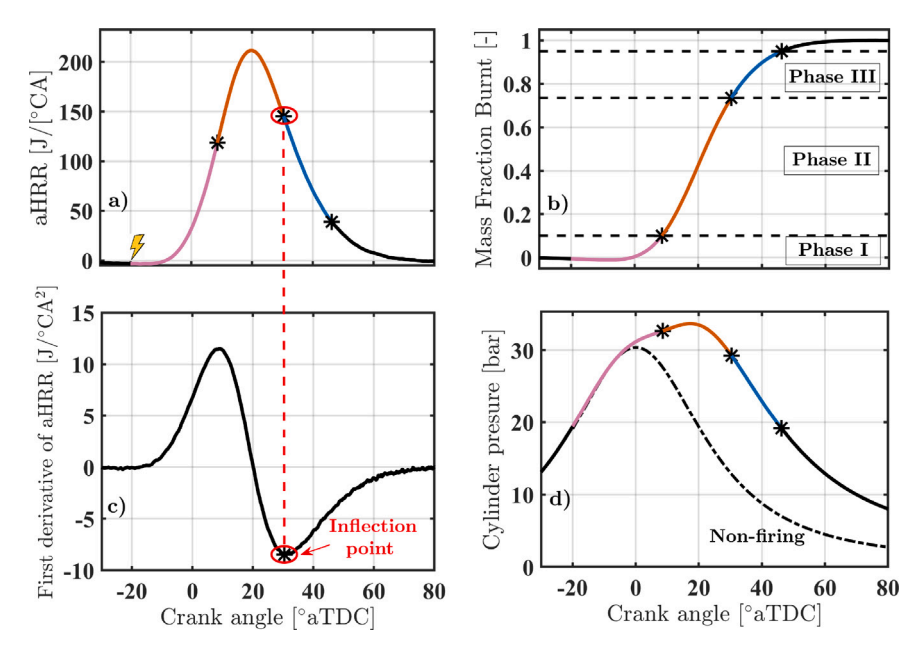


Fig. 6. Definition of combustion phases for the converted NG-SI used in this study.

burning may contribute to the slightly better efficiency observed in cylinder 7, it is challenging to draw definitive conclusions due to the influence of gas path dynamics, which leads to different boundary conditions for each individual cylinder. As expected, Fig. 7e shows that the mean cylinder exhibits lower COV levels; notably, it also lacks a prominent late combustion phase across all cycles. This could be attributed to the fact that, at least for this operating point, the engine rarely encounters more than one cylinder exhibiting significantly delayed combustion simultaneously, resulting in effective averaging and balancing across the cylinders.

Therefore, although the average heat release rates demonstrate that late combustion is nonconsistent across both cycles and cylinders, it is evident that relying solely on average values, either a mean cycle or a mean cylinder, can hide the real combustion profile that might occur in some cycles or cylinders. Nevertheless, average profiles still offer valuable insights into the overall combustion characteristics of the engine. While this study primarily focuses on comparing the mean heat release profile of the mean cylinder across different operating points, individual profiles should be analyzed when necessary to provide a more detailed understanding.

Combustion characteristics can vary significantly across different load points, especially in throttle-valve controlled systems like this particular concept. Fig. 8 presents in-cylinder pressure, heat release, bulk gas temperature, and mass fraction burnt across the load sweep. As expected, both pressure and heat release increase with load, and combustion phasing remains consistent across most load points, except for the lowest load of 100 kWe, which shows advanced combustion. The MFB plot in Fig. 8c demonstrates this advancement at the lowest load, which can be attributed to greater flame propagation speeds resulting from richer mixtures used as nominal conditions at this load to address low-load combustion stability challenges [13].

These richer mixtures at the low load point also lead to the highest bulk gas temperatures in the cylinder, as seen in Fig. 8b, which can be confirmed by out-cylinder temperature measurements across all cylinders and the manifold. This subsequently results in advanced phasing for the whole combustion process and all individual defined combustion stages at 100 kWe load. Fig. 8c highlights the transition points between the defined combustion stages. The consistent advancement of both the bowl-in and squish combustion stages contrasts with the anticipated trend of squish combustion deterioration observed with advanced combustion phasing in converted SI engines. However, at least

20% of the fuel combusted during the slower squish combustion stage across the lean operating load points. Minimizing this phenomenon is crucial, as it significantly impacts both thermodynamic and combustion efficiency in these engine concepts. Additionally, the phase markers indicate consistent combustion phasing across all load points operating under similar dilution levels, with the exception of a slight delay in the combustion duration at the lowest load of 200 kWe.

# 4.2. Performance and emissions characteristics

Conducting a comprehensive combustion analysis of multicylinder engines necessitates a thorough examination of the energy balance. This aspect is critical for the current engine concept, as it can provide insights into how distinct combustion stages influence overall energy distribution. Analyzing, first, the energy share at the baseline load points is important to better understand the effects of different parameters and combustion stages on overall engine performance. In this study, the energy balance for the representative mean cylinder is analyzed across all operating points. A Sankey diagram, as illustrated in Fig. 9 for the 200 kWe operating load point, offers a visual representation of this energy balance and its key components. Fuel slip in the exhaust, heat transfer through the cylindrical boundaries, energy in the exhaust gases, pumping, and friction losses are the typical components of energy losses in a reciprocating ICE.

Fig. 10 collects the key fuel energy components across operating points and presents the energy distribution for the tested load sweep. As anticipated, friction losses decrease with increasing load. Since the engine speed remains constant, the relative share of friction losses in relation to the fuel energy input also diminishes. Pumping losses follow a similar trend, decreasing at higher loads, which is typical for such throttle valve-controlled engines, particularly those equipped with a turbocharging system which are more efficient at higher loads, utilizing some exhaust gas energy to lower pumping losses. A decreasing pattern is also observed for heat losses from the cylindrical boundaries as load increases. The higher level of heat losses at the lowest load can be attributed to the higher bulk gas temperature. Although bulk gas temperatures are relatively higher at the highest load, as shown in the zoomed section of Fig. 8b, leading to greater cumulative heat transfer, the relative heat transfer losses decrease when compared to the increasing energy input. This trend is further supported by the heat loss model coefficient  $C_0$ , which consistently decreases from 228.9 at 200

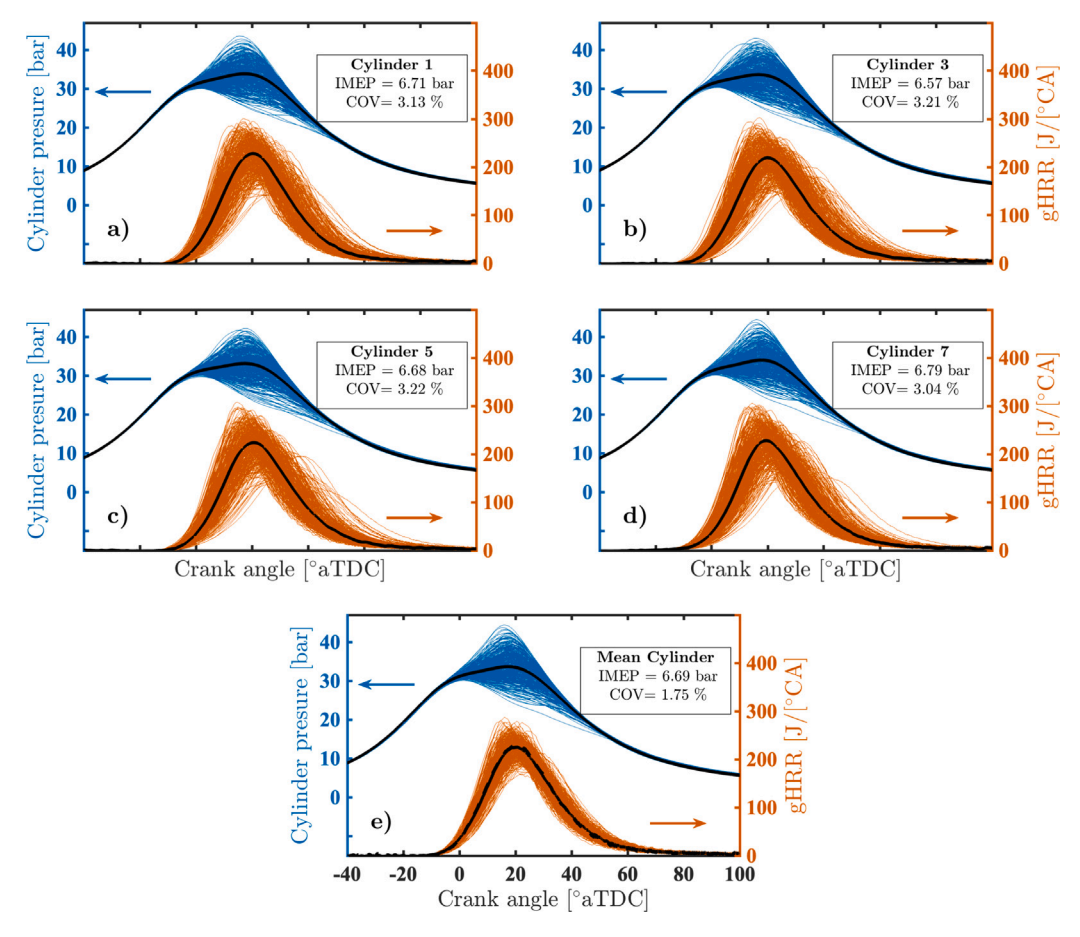


Fig. 7. Cycle-by-cycle variation of pressure and heat release rate across all and mean cylinders for Case 2.

kWe to 193.2 at 432 kWe load point. Table 8 in Appendix B presents the calibrated coefficients for the tested operating conditions. Exhaust gas losses, on the other hand, increase at higher loads due to the greater enthalpy associated with the increased mass flow rates and temperature of exhaust gases.

Methane emissions remain one of the main challenges in such engine concepts due to both its impact on both the environment and the engine performance. In this study, energy losses due to unburned fuel, or fuel slip, remain fairly constant across all operating points, ranging from 2.26% to  $2.76\% \pm 1.67\%$ , with the lower fuel slip occurring at the highest load point. This slightly better combustion performance might be attributed to a better combination of thermal conditions and oxygen quantity for the conversion of the fuel. However, drawing definitive conclusions regarding the load effect is challenging when considering the associated uncertainty levels. Additionally, the relatively consistent levels of fuel slip across all loads might be a result of the fuel trapped in the crevice regions of the chamber. Consequently, these trends in energy distribution result in a typical increase in overall engine efficiency as the load increases Specifically, brake thermal efficiency (BTE) increases 22.39%  $\pm$  0.33% at the lowest load point (100 kWe) to  $33.91\% \pm 0.36\%$  at the highest load point (432 kWe).

Fig. 11 illustrates the emission characteristics of the engine across the tested load sweep. Among the emissions considered,  $\mathrm{NO}_{x}$  is the only regulated emission for maritime engines by the International Maritime Organization (IMO) [72], while methane regulations are still under development [50]. The rated amount of the IMO Tier III standards  $\mathrm{NO}_{x}$  emissions for this engine is 2.08 g/kWh, which would correspond to the weighted average over a standardized test cycle, e.g., D2 for marine generator sets. This study presents  $\mathrm{NO}_{x}$  values for each individual load point tested and indicate this Tier III standard for reference. To this end, it should be noted that direct comparison of single-point emissions

to the Tier III standard may be misleading when the compliance of the engine is assessed. When considering the weighted average of the tested operating points across the load sweep, this engine meets Tier III  $\rm NO_x$  requirements under nominal conditions. However, at the lowest load,  $\rm NO_x$  emissions reached 2.79  $\pm$  0.19% g/kWh, exceeding the single-point Tier III value, while all other tested loads remained below the standard.

The elevated  $\mathrm{NO}_{\mathrm{x}}$  at the lowest load is attributed to the use of a relatively richer mixture, which increases combustion temperatures, as reflected in Fig. 8b. This richer mixture at low load also resulted in the poorest combustion efficiency and the highest emissions of CO, CH<sub>4</sub>, and total UHC. This demonstrates the effectiveness of lean-burn operation for controlling  $\mathrm{NO}_{\mathrm{x}}$ . Across the remaining load points,  $\mathrm{NO}_{\mathrm{x}}$  emissions remained relatively stable but showed a slight upward trend with increasing load from 200 to 432 kWe. Since combustion phasing, air excess ratio, and bulk gas temperatures were similar across this range, the observed increase is likely due to higher mass flows at elevated loads, resulting in increased oxygen and nitrogen density, which can promote additional  $\mathrm{NO}_{\mathrm{x}}$  formation.

Although slight variations in air excess ratio were present across load points, the effect of load on emissions is clear: increasing load improves combustion efficiency, albeit with a modest rise in  $\rm NO_x$  formation. Methane slip aligned well with the expected range for LBSI marine engines [50]. Among current marine engine strategies using natural gas, LBSI engines — most commonly with pre-chamber designs [73] — and low-pressure dual-fuel (LPDF) engines are prominent. Notably, the open-chamber LBSI configuration employed here, despite its simplicity, achieves methane emission levels comparable to more advanced pre-chamber SI engines. This finding is significant for retrofitting existing diesel engines to SI operation, where design simplicity and cost-effectiveness are priorities. At high loads (400 and 432 kWe), methane emissions were recorded 3.21  $\pm$  0.13% and 3.01

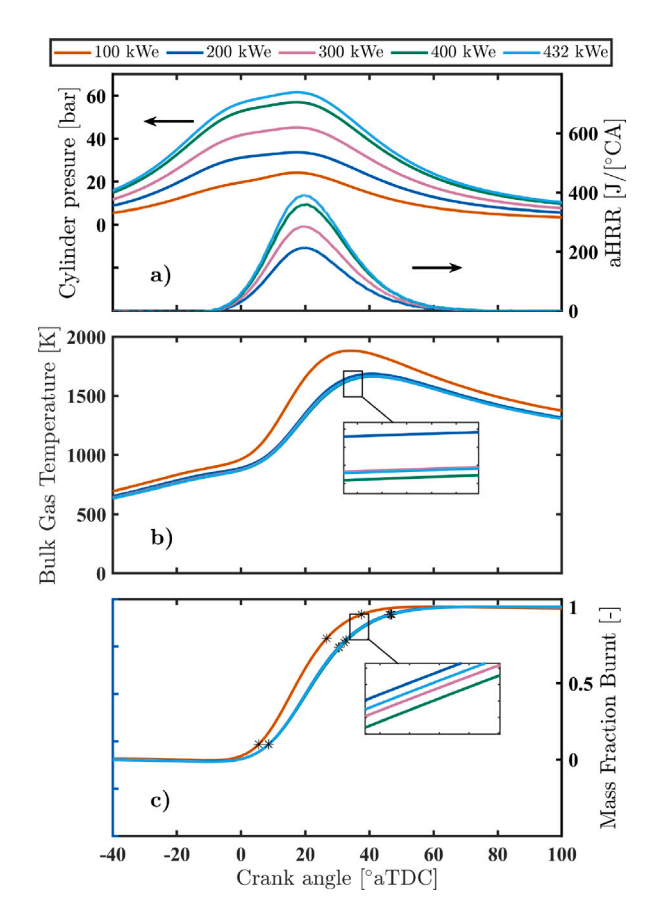


Fig. 8. Effect of load on pressure and heat release rate (a), bulk gas temperature (b) and mass fraction burnt (MFB) (c).

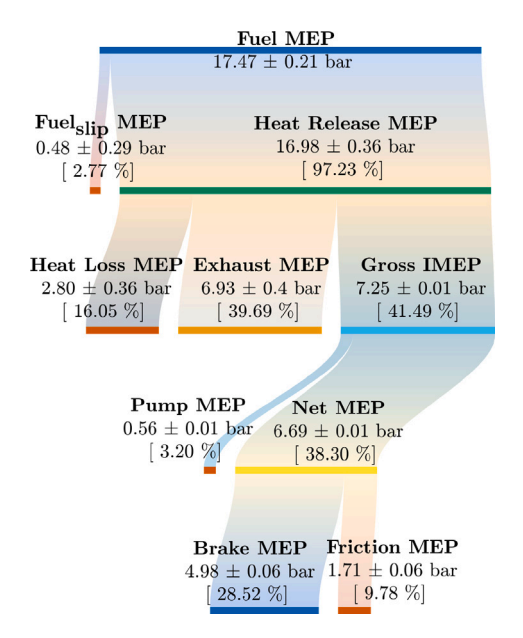


Fig. 9. Energy balance of the mean cylinder using the Sankey diagram for the 200 kWe load point.

Source: Adapted using the Sankey plot script created by Liu [71].

 $\pm$  0.12% g/kWh, respectively, which falls within the typical 3–5 g/kWh range for pre-chamber LBSI engines and the broader 3–10 g/kWh range for LPDF engines [50]. At lower loads (100, 200, and 300 kWe), methane emissions ranged from 3.69  $\pm$  0.15% to 4.59  $\pm$  0.20% g/kWh,

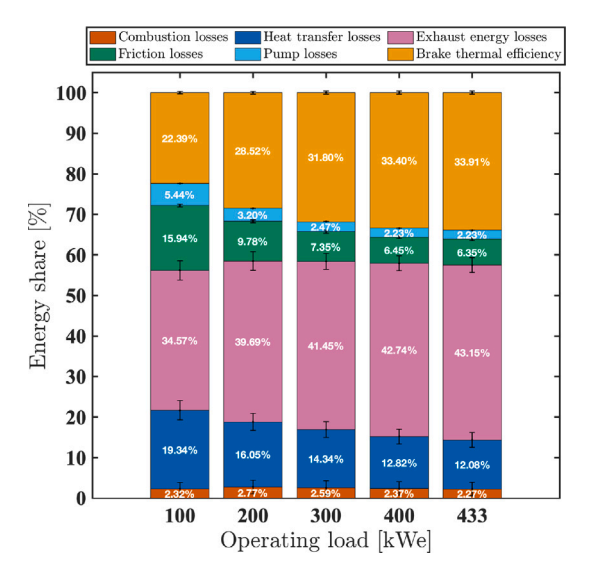


Fig. 10. Energy share across load points.

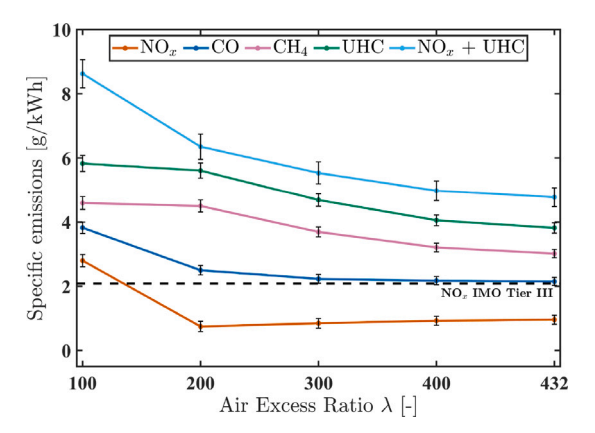


Fig. 11. Emissions across load points.

again within the anticipated 3.3–7.2 g/kWh range, and well below the much higher values occasionally reported for these engine types at very low loads. These results highlight the capability of open-chamber lean-burn engines to achieve low  $NO_{\rm x}$  with acceptable combustion performance and methane slip at low loads.

Furthermore, the sum of UHC and  $NO_x$  emissions — a metric often referenced in emissions legislation [16] but not yet implemented in marine regulations — also exhibits a clear decreasing trend with increasing load. Future regulatory frameworks should incorporate holistic assessment methods that enable fair comparison of different engine strategies, including LBSI and DF engines, and consider not only  $NO_x$  and methane but also relevant pollutants such as soot, which is particularly relevant for diesel and DF engines. Such comprehensive evaluations will be essential for appropriately assessing and encouraging the adoption of alternative fuel engine concepts in the maritime sector, including simplified retrofitting solutions based on single-fuel LBSI strategies.

#### 4.3. Air excess ratio effects

The high-turbulence induced by the distinct combustion chamber geometry offers advantages over conventional SI engines due to its ability to operate with high levels of dilution. This capability can simultaneously reduce  $\mathrm{NO}_{\mathrm{x}}$  emissions due to lower temperatures while enhancing combustion efficiency, i.e., lower CO and UHC emissions,

Table 5
Main combustion characteristics of the distinct combustion stages.

Air excess λ [–] Flame development		Bowl-in phase II			Squish phase	CD [°CA]		
	phase I [°CA]	CAD [°CA]	Fuel burnt [%]	Average temperature [K]	CAD [°CA]	Fuel burnt [%]	Average temperature [K]	
1.25	23.1	16.9	67.9%	1520	10	17.2%	2000	26.9
1.38	24.6	18.4	66.8%	1455	11.2	18.1%	1882	29.6
1.45	26.2	19.8	66.4%	1404	12.4	18.6%	1793	32.2
1.5	27.4	21.8	68.0%	1388	12.4	16.9%	1744	34.2
1.57	29.1	21.8	63.5%	1324	15.8	21.4%	1669	37.6
1.59	29.3	24.6	66.3%	1315	15.6	18.7%	1626	40.2
1.65	31.1	26.5	62.6%	1250	21.9	22.4%	1528	48.4
1.71	31	30.1	61.8%	1203	29.1	23.2%	1434	59.2
1.77	31.2	31.9	62.3%	1180	31.4	22.6%	1388	63.3

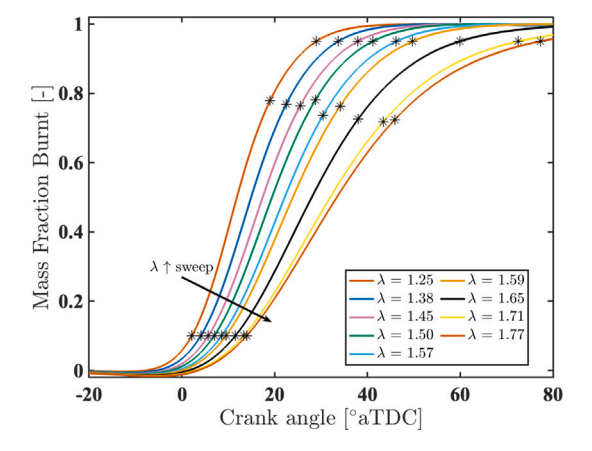


Fig. 12. Mass fraction burnt across the air excess ratio  $\lambda$  sweep.

due to greater oxygen availability. However, there is a threshold beyond which excessive dilution leads to very low temperatures, negatively impacting combustion efficiency. The distribution of fuel burned across the different combustion stages can significantly influence the overall fuel conversion efficiency and emissions characteristics. This study swept the air excess ratio from  $\lambda$  of 1.25 to 1.77 at constant engine speed, generator load, and spark timing.

Fig. 12 illustrates the mass fraction burnt across the operating points during the air excess ratio sweep. Table 5 presents the quantified combustion characteristics of the defined combustion stages at different air excess ratios, including duration, the amount of fuel burned, and the average bulk gas temperature for each phase. The phasing methodology, based on the ensemble average of 400 consecutive cycles across four cylinders, demonstrates minimal uncertainty in phase boundary identification derived from the aHRR profile (Section 3.3). To this end, the uncertainty range for the different phases, thus the fuel burnt in each phase, is negligible and omitted from tables/texts for brevity. Further, as the engine increased fuel mass flow to compensate the apparent decrease in IMEP with leaner mixtures, it also increased the air mass flow to maintain the requested air excess ratio, which resulted in greater mass flow through the engine and slight changes in boundary conditions. These adjustments introduce some complexities when comparing performance across different air excess ratios. The same considerations apply to all parametric sweeps conducted in this study. However, adjustments do not diminish the study's ability to derive valuable insights into the impact of different parameters, such as dilution, on combustion characteristics and engine performance.

An extension in combustion duration is evident across all defined combustion phases during the leaning sweep, consistent with trends observed in conventional SI engines, due to reduced flame speed associated with leaner mixtures. Flame development phase I consistently increased across the leaning sweep from 23.1 to 31.2 °CA, as it is strongly influenced by laminar flame speed, a property highly sensitive to air-to-fuel ratios. The observed duration of flame development was

longer than that reported in experiments with combustion chambers of similar geometric characteristics [16]. This can be attributed to the leaner NG composition used in this engine, as well as potential differences in ignition system configurations. Regarding the main combustion phase, the flame propagated more rapidly during both main combustion phases (Phases II and III) in richer mixtures, contrary to the anticipated slowing effect expected due to the larger surface-to-volume ratio in the squish region, as observed in previous experimental studies, e.g., in [36]. Diluting the mixture from  $\lambda$  of 1.25 to 1.77 increased the duration of Phase II from 16.9 °CA to 31.9 °CA, representing an increase of 89%, and Phase III from 10 °CA to 31.4 °CA, an increase of 214%. Combustion duration, therefore, showed a clear increasing trending with leaner mixtures, increasing from 26.9 °CA at  $\lambda$  of 1.25 to 63.3 °CA at  $\lambda$  of 1.77. This trend in overall combustion phasing and duration, including the individual squish combustion phase, demonstrates that enriching the mixture clearly outweighs the expected negative impact of the larger surface-to-volume ratio on the flame propagation in the squish region. The higher squish height in this engine's combustion chamber compared to the previous studies could explain the diminished effect of the surface-to-volume ratio on the flame speed in the squish region. The use of highly diluted and lower methane number NG in the experiments also plays a role in moderating flame propagation and extending it during the expansion phase. This results in flame propagating through the squish region at a later stage, where the surface-to-volume effect decreases. Interestingly, the sensitivity of the main combustion phase to air excess ratio in this engine is significantly higher than what is typically expected for a hemispherical piston bowl [16]. This is likely attributed to the distinct combustion chamber geometry in this setup, differing from this typical hemispherical shape featuring characteristics intermediate between a turbine bowl and a hemispherical design, with an extended squish are.

The amount of fuel burned across the two stages appears less sensitive to the dilution sweep tested compared to their phasing. While the trend is clear for the fuel distribution in the two phases from the richest to the leanest mixture, this trend is not consistent in the intermediate air excess ratios tested. A slight increase in the amount of fuel burned during the rapid combustion stage is even observed at some intermediate  $\lambda$  values compared to the richest mixture. It is difficult, however, to conclude that more fuel was actually consumed within the bowl for these leaner mixtures. Slower combustion rates associated with leaner mixtures can lead to greater overlap between the two distinct combustion stages, potentially causing a larger portion of the squish combustion heat release to be classified as part of the Phase II under the current methodology. This has been demonstrated and further discussed in a parallel study on this experimental campaign [74], as well as in previous studies with similar chamber geometries [75]. Nevertheless, it is clear that enriching in-cylinder mixture consistently improves combustion conditions for both phases. Richer mixtures, characterized by lower heat capacities, lead to more fuel being combusted faster, closer to TDC, and at higher temperatures, resulting in higher combustion and thermodynamic efficiency.

The efficiency improvements are corroborated by Fig. 13, which demonstrates a consistent improvement in combustion efficiency along

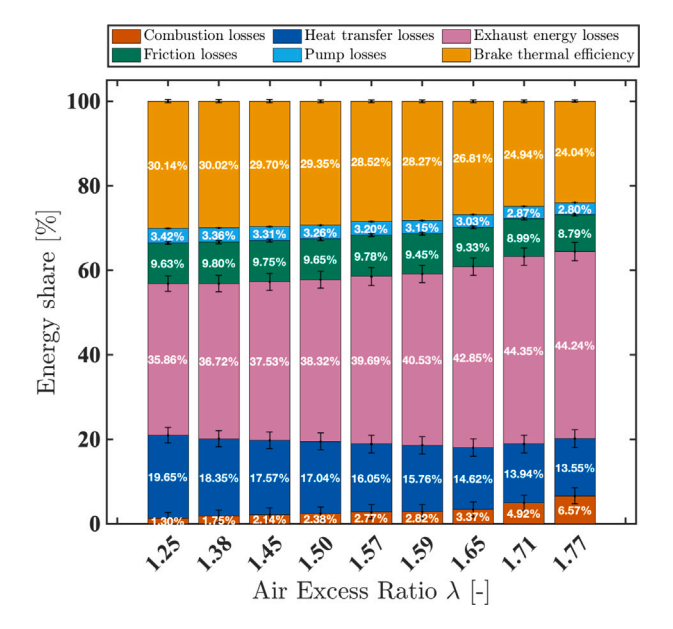


Fig. 13. Energy share across the air excess ratio sweep.

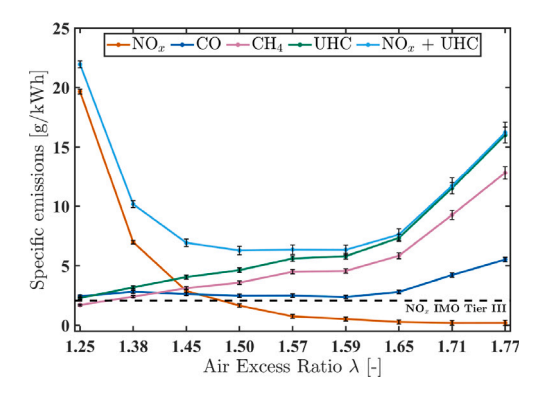


Fig. 14. Emissions across the air excess ratio sweep.

the dilution sweep, as the fuel slip energy share decreased from 6.57%  $\pm$  1.95% at the leanest mixture to 1.30%  $\pm$  1.30% at the richest. Brake thermal efficiency followed a similar trend increasing by 25% across the whole enrichment sweep, despite the anticipated increase in heat losses, as friction and pumping losses remaining relatively constant across all tested air excess ratios. The improvement in efficiency could be anticipated even before conducting the energy analysis, as the engine's controller compensates for the lower IMEP in the cylinders by increasing fuel input to maintain the generator load. The lower IMEP is caused by the decrease in thermodynamic efficiency from the more delayed combustion phasing [55].

Regarding emissions performance, Fig. 14 demonstrates an inverse relationship appears between  $NO_x$  and UHC emissions. While richer mixtures resulted in the higher combustion efficiency across the tested air excess ratios, they also led to a significant rise in  $NO_x$  emissions due to higher combustion temperatures. The three richest mixtures tested resulted in  $NO_x$  levels exceeding the IMO Tier III standards, even though they achieved the lowest methane, total UHC, and CO emissions. Within the range of  $\lambda$  values between approximately 1.50 and 1.65, the sensitivity to dilution appears lower, offering a relatively stable trade-off between  $NO_x$  and combustion efficiency. This is corroborated from the trend of the sum of  $NO_x$  and UHC that demonstrate the lowest levels in this range. Beyond this range, further enrichment result in a sharp increase in  $NO_x$  emissions, while additional leaning beyond  $\lambda$  of 1.65 leads to significant combustion inefficiency and high levels of

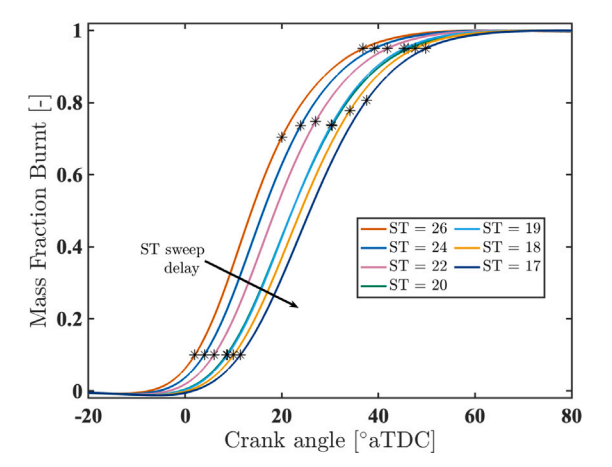


Fig. 15. Mass fraction burnt across the spark timing (ST) sweep.

UHC emissions. The sensitivity of emissions characteristics and the optimal air excess ratio range for balancing emissions align with findings from previous experimental studies comparing different combustion chambers for gas engines [16]. Consequently, for this operating load point of the engine, an air excess ratio between 1.45 to 1.60 appeared to offer the optimal balance between combustion efficiency and  $\rm NO_x$  emissions, maintaining the sum of  $\rm NO_x$  and UHC emissions below 6.5 g/kWh. Given the critical impact of emissions like methane, this trend underscores the need to develop comprehensive standards that account for the combination of multiple critical emissions in marine gas engines.

#### 4.4. Spark timing effects

Spark timing has always been a critical input parameter for controlling combustion phasing, efficiency, and emissions in SI engines. For this specific engine concept, spark timing has been found to have a distinct impact compared to conventional SI engines, influencing the different combustion phases and, consequently, overall engine performance. This subsection examines the effect of a spark timing sweep on combustion characteristics and engine performance under constant engine speed, generator load, and air excess ratio.

Fig. 15 illustrates the mass fraction burned across the operating points during the spark timing sweep, with Table 6 quantifying the associated combustion characteristics. Unlike the effect of air excess ratio, spark timing sweep showed varying impacts across the defined combustion phases. Delayed spark timing clearly delayed flame development and bowl-in phases, aligning with the anticipated behavior in conventional SI engines. The main combustion phase and total combustion duration exhibited a clear and consistent increase with delayed spark timing, rising from 18 °CA to 26.2 °CA and 34.8 °CA to 38.4 °CA, respectively. On the other hand, the squish combustion phase (Phase III) displayed an opposite trend advancing from 16.8 °CA to 12.2 °CA. Notably, the operating point with spark timing at 20 °CA bTDC appears as a slight outlier in most observed trends, likely due to a slightly higher air excess ratio at this point. The offsetting effect of delayed spark timing on the total combustion duration by the enhanced squish phase is corroborated in Fig. 15, where the phasing difference between different spark timing configurations diminishes from the end of the bowl-in phase to the end of the squish combustion stage. This behavior aligns with observations from previous optical studies of this type of SI strategy, which highlights that flame propagation improvements are limited in the squish combustion stage due to higher surface-to-volume ratios counteracting flame propagation. While this effect can reduce or even reverse the benefits of spark timing advancement, as reported in earlier experimental studies, the slower squish combustion stage in this engine does not negate the benefits of spark advance. Advancing spark

Table 6
Main combustion characteristics of the distinct combustion stages across ST sweep.

Spark timing	Flame development	Bowl-in phas	Bowl-in phase II			Squish phase III			
ST [°CA bTDC]	phase I [°CA]	CAD [°CA]	Fuel burnt [%]	Average temperature [K]	CAD [°CA]	Fuel burnt [%]	Average temperature [K]		
26	22	18	60.5%	1361	16.8	24.6%	1691.4	34.8	
24	24.5	19.9	63.5%	1376	15.3	21.4%	1675.6	35.2	
22	26.2	21	64.7%	1362	14.9	20.2%	1661.3	35.9	
20	29.1	21.8	63.5%	1335	15.8	21.4%	1620.3	37.6	
19	28.9	21.5	63.8%	1331	15	21.1%	1646.0	36.5	
18	29.6	24.1	67.9%	1335	13.5	17.2%	1639.7	37.6	
17	31.8	26.2	70.8%	1348	12.2	14.3%	1624.1	38.4	

timing shifts combustion phasing closer to TDC, enabling more fuel to be burned under thermodynamically favorable conditions, as evidenced by the CA50 advancement from 27.4 to 15.6 °CA aTDC during the ignition timing sweep, enhancing the pressure exerted during the early stage of the power stroke.

The observed increase in the mass fraction burned during the rapid combustion phase (Phase II) with delayed spark timing, rising from 60.5% to 70.8%, likely suggests that delayed ignition prolongs combustion within the bowl-in and squish phases. This overlap complicates the attribution of fuel burned to each phase, as some of the heat release classified as bowl-in may in fact occur during the early squish phase period. Consequently, the redistribution of fuel burning between phases is not always clearly distinguished, and definitive trends are difficult to establish based on pressure-derived data. Despite these complexities, the overall trend remains that later spark timing delayed overall combustion phasing, thereby deteriorating efficiency.

These improvements are corroborated by the observed performance improvements across the spark timing sweep, as shown in Fig. 16, further emphasizing the importance in optimizing combustion phasing and overall engine performance. Despite the improvement in overall thermal efficiency of the engine, a 10% increase across the spark timing advancement sweep, there appears a consistent increase in combustion efficiency, rising from 97.14% at 26 °CA bTDC to 97.62%  $\pm$  1.63% at 17 °CA bTDC. It is challenging, however, to draw definitive conclusions regarding methane emissions improvement with spark timing delay with such minor differences, considering the varying mass flows and the inherent uncertainties in the measurement system. It is evident that spark timing influences combustion efficiency differently than air excess ratio. Within the range tested, spark timing demonstrated limited impact, with the generally anticipated benefits of advanced timing, even potentially deteriorating combustion efficiency. This behavior highlights the differences between this homogeneous LBSI strategy and conventional/pre-chamber SI systems. In conventional SI engines with flat piston geometries, advancing spark timing typically improves combustion efficiency by shifting combustion closer to TDC and more favorable thermodynamic conditions (until knock limit), as the absence of a squish phase eliminates sensitivity to late-stage flame propagation. The closer to TDC combustion, therefore, maximizes the pressure exerted on the piston during the power stroke. In contrast, pre-chamber SI systems, even when using similar chamber geometries as this LBSI concept, can mitigate squish region limitations through charge stratification. In such concept, fuel-richer mixtures near the spark plug enhance ignition energy transfer to the charge in the main chamber, while also reducing the amount of fuel present in the squish region. Given the critical importance of methane emissions in gas engines, these findings underscore the need for careful consideration of combustion phasing in the design and control strategies for such SI concepts.

Similar to the increasing air excess ratio, delayed spark timing led to higher exhaust gas energy share. This can be attributed to more delayed combustion phasing in both sweeps that result in hotter exhaust gases. This, in turn, slightly reduced pumping losses because of greater turbocharging power. Heat transfer processes exhibited minimal sensitivity, with a slight decrease observed as spark timing was delayed due to lower maximum bulk gas temperatures. Therefore, although it

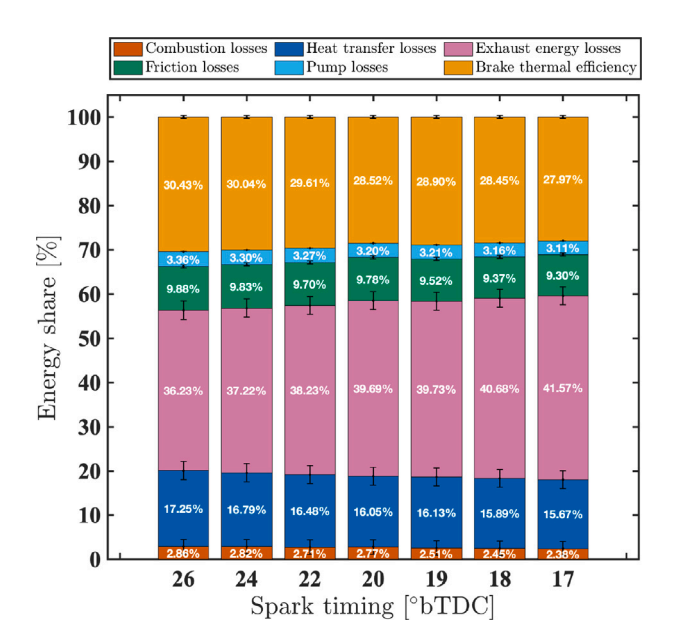


Fig. 16. Energy share across the spark timing sweep.

is challenging to clearly determine the effect of spark timing in the engine performance characteristics, including combustion efficiency, due to different mass flows, the lower fuel slip energy share under these conditions suggest that delayed spark timing might slightly improve squish combustion phase, thereby improving overall fuel conversion efficiency.

Fig. 17 illustrates the emissions characteristics across the spark timing sweep. All measured emissions decreased with delayed spark timing, with hydrocarbon related emissions aligning with the earlier discussion on improved combustion efficiency. This further highlights the distinct, and different from the conventional SI, sensitivity of this strategy to spark timing. Methane emissions decreased from  $4.25 \pm 0.23$ to 3.84  $\pm$  0.20 g/kWh, CO from 2.56  $\pm$  0.14 to 2.18  $\pm$  0.15 g/kWh, and total UHC emissions from 5.42  $\pm$  0.18 to 4.92  $\pm$  0.16 g/kWh. Additionally, all tested spark timings met the IMO Tier III standards for NO<sub>v</sub> emissions except the most advanced setting at 26 °CA bTDC. Delaying spark timing consistently reduced NO<sub>v</sub> levels from 2.37  $\pm$  0.15 to 0.59 + 0.16 g/kWh, which can be attributed to the lower temperatures during the main combustion phases, as shown in Table 6. The critical metric of the sum of NO<sub>x</sub> and UHC emissions clearly decreases with more delayed ignition timing. Interestingly, while the most advanced spark timing settings led to more advanced combustion phasing and higher brake thermal efficiency, they did not improve combustion efficiency but instead caused a decline. Therefore, an increase in BTE does not necessarily indicate improved combustion performance in these SI engines. This can be attributed to the deterioration of the squish phase at advanced spark timings and the high sensitivity of combustion performance to this phase in such engines.

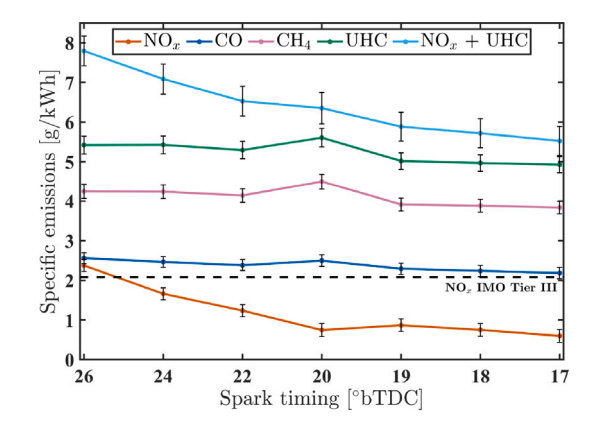


Fig. 17. Emissions across the spark timing sweep.

These results demonstrate that while richer mixtures enhanced combustion efficiency, advanced spark timing did not yield the same benefits in the squish phase. Despite both the most advanced spark timing (ST = 26 °CA bTDC) and richest mixture ( $\lambda$  = 1.25) configurations resulting in flame reaching the squish region at similar timing, richer mixtures achieve superior flame propagation, with squish combustion phasing differing by over 10 °CA between the two cases. This discrepancy arises from the limited effectiveness of turbulent kinetic energy (TKE) in the squish region, where flame's surface-to-volume ratio dominates over turbulence effects. Advanced spark timing enhances flame propagation in the bowl-in region, even under lean mixtures, by leveraging favorable thermodynamic conditions near TDC and elevated TKE induced by the combustion chamber geometry. While TKE partially compensates for lower laminar burning velocities under lean mixtures in the bowl-in region, its influence due to piston position diminishes in the squish region. Here, flame surface area becomes the critical factor. Richer mixtures, inducing higher laminar burning velocities, develop larger flame surface areas, thereby turbulence-aided flame speeds, enabling them to overcome the squish region's constraints more effectively than spark timing adjustments. Consequently, the interplay between the two control parameters is also expected to be very important for the optimization of combustion efficiency, thereby UHC emissions including methane. Given the concerns surrounding methane, these findings underscore the need for a Designof-Experiment (DoE) approach to systematically evaluate interactions between control parameters and optimize this SI engine concept [76].

# 4.5. Intake temperature effects

Intake air temperature is another critical parameter that influences engine performance, primarily by affecting air density within the cylinder [34]. Although air temperature is particularly important for liquid fuels like methanol, which face evaporation and mixture formation challenges, this research conducted an intake air temperature sweep to assess its impact on combustion and performance characteristics. Such insights are valuable for comparative analysis of similar engine concepts operating on different fuels, including the planned conversion of this engine to run 100% on methanol. The intake air temperature was controlled using a three-way valve in the intercooler to explore its effects under constant engine speed, generator load, and spark timing. This study shows the estimated temperature at IVC to demonstrate the resulting intake air temperature sweep.

Maintaining consistent air excess ratio throughout this sweep was not feasible, as the engine required adjustments to both fuel flow and throttle valve position to sustain the generator load during the test. These adjustments were necessary due to the inability of the engine control system to maintain a constant load at a fixed engine speed. Although this might raise questions about the control strategy

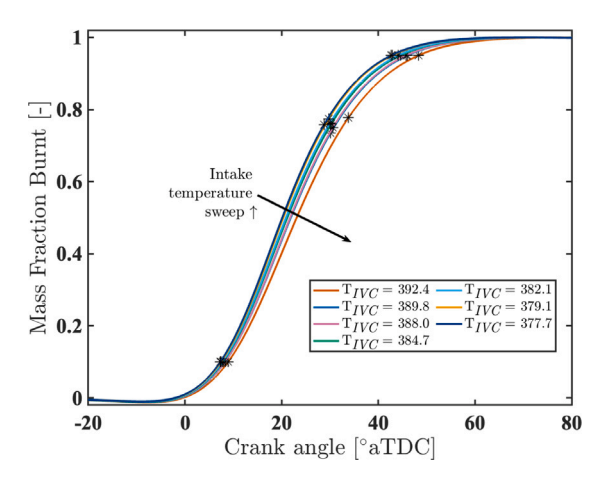


Fig. 18. Mass fraction burnt across the intake temperature sweep.

and its effectiveness in optimizing fuel and air inputs, the observed adjustments provide some preliminary indications of improved engine efficiency at lower intake air temperatures.

The intake air temperature sweep range conducted in this study had the smallest effect on combustion performance compared to both spark timing and air excess ratio, as shown in Fig. 18. Table 7 quantifies the impact of intake air temperature on distinct combustion phases and their characteristics. Increasing intake air temperatures from 375.7 K to 390.6 K at IVC prolonged all defined combustion phases, with combustion duration rising from 35.3 °CA to 39.4 °CA. The distinct phases II and III increased from 21.5 °CA to 24.9 °CA and 13.8 °CA to 14.5 °CA, respectively. Although higher intake air temperatures increased in-cylinder temperatures at IVC, the larger amount of fuel and corresponding increase air excess ratio induced by the controller inputs, resulted in lower average bulk gas temperatures during both distinct combustion phases at higher intake air temperatures. These lower bulk gas temperature can be attributed to larger heat capacities and slightly delayed combustion phasing with increased intake air temperatures. Fuel distribution across two main combustion phases remained relatively insensitive to intake air temperature changes, with only a clearer slight decrease observed in the fuel mass burned during Phase II. However, the potential overlap between combustion phases, expected with combustion phasing delay, makes it challenging to draw definitive conclusions about the influence of intake air temperature on fuel distribution in the combustion chamber.

This improvement with lower intake air temperature is also corroborated by the distribution of the fuel energy across the main fuel energy components, as seen in Fig. 19. As anticipated from the fuel flows measurements across the temperature sweep, brake thermal efficiency exhibited a consistent decrease from 29.32% to 28.55%  $\pm$  0.35% along the increasing intake air temperature steps taken. The improvement in brake thermal efficiency was achieved despite the slight increase in energy losses through friction, pumping, and heat transfer with lower intake air temperatures. The higher pumping losses can be attributed to the more advanced combustion phasing and lower mass flow rates of exhaust gases that result in decreasing turbocharging power.

The observed higher average bulk gas temperatures and advanced combustion phasing at lower intake air temperatures increased combustion efficiency from 97.1% to 97.56%  $\pm$  1.67%, while this also increased heat transfer energy share from 16.02% to 16.65%  $\pm$  2.06%. This improvement translated into enhanced combustion performance, as observed in the decreasing trends of methane and UHC emissions in Fig. 20. Methane decreased from 4.65  $\pm$  0.19 to 3.71  $\pm$  0.15 g/kWh, with total UHC emissions reducing from 5.90  $\pm$  0.24 to 4.79  $\pm$  0.20 g/kWh. However, as noted in Sections 4.3 and 4.4, there remain reservations about drawing definitive conclusions regarding the influence of

Table 7

Main combustion characteristics of the distinct combustion stages across intake temperature sweep.

Temperature at	Flame development	Bowl-in phas	Bowl-in phase II			Squish phase III			
IVC [K]	phase I [°CA]	CAD [°CA]	Fuel burnt [%]	Average temperature [K]	CAD [°CA]	Fuel burnt [%]	Average temperature [K]		
392	28.3	24.9	67.8%	1347	14.5	17.3%	1650	39.4	
390	28.1	21.8	63.5%	1335	15.9	21.5%	1672	37.7	
388	28.1	22.3	64.9%	1345	15.1	20.0%	1679	37.4	
385	28	22.4	66.1%	1352	14.3	19.0%	1690	36.7	
382	28.6	22.2	66.2%	1355	14.1	18.7%	1697	36.3	
379	27.4	22.2	67.3%	1365	13.2	17.7%	1712	35.4	
378	27.9	21.5	65.9%	1355	13.8	19.1%	1712	35.3	

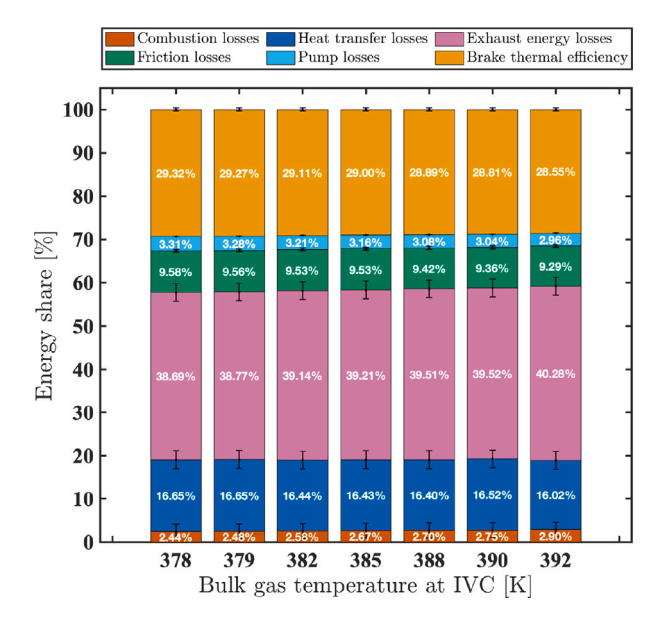


Fig. 19. Energy share across the intake temperature sweep.

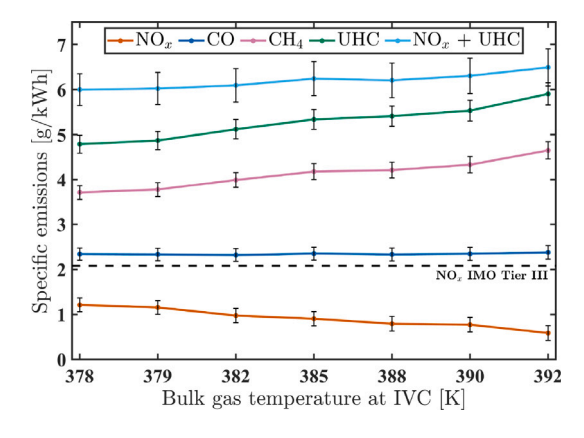


Fig. 20. Emissions across the intake temperature sweep.

intake air temperature on these quantified emissions characteristics. CO emissions remained relatively stable during the intake air temperature sweep, likely due to counteracting effects: higher oxygen concentration and lower in-cylinder temperatures. NO $_{\rm x}$  emissions exhibited the expected opposite trend with CH $_{\rm 4}$  and UHC emissions, increasing from 0.58  $\pm$  0.17 g/kWh at 392 K to 1.21  $\pm$  0.15 g/kWh at 378 K. Overall, the trend in the sum of NO $_{\rm x}$  and UHC emissions clearly indicates that higher air density, achieved with lower intake air temperatures, enhances combustion performance.

#### 4.6. Phasing and engine performance

Following the assessment of individual trends with each control parameter, it is important to isolate the influence of combustion phasing metrics on key performance indicators across all tested operating points. Fig. 21 presents the trends of several engine performance metrics as functions of the inflection point — approximating the end of the bowl-in and the start of the squish phase — and the fuel burnt into ratio across these two phases. It should be noted that this figure is intended to illustrate general trends among various engine performance indicators, rather than to provide predictive relationships, since it is based on a limited number of discrete operating conditions.

The summarized results clearly indicate that the inflection is a more critical influencing factor than the fuel burnt ratio for all performance indicators. This observation aligns with previous findings, as no distinct trend was found in fuel distribution across the two main combustion phases. This might be attributed to the overlapping phenomenon between the two stages. However, a certain influence can be observed, with lower fuel squish-to-bowl ratio leading to better combustion performance decreasing methane emissions while increasing heat losses and NO<sub>x</sub> emissions. The effects in COV and BTE is less clear.

On the contrary, the impact of the inflection point on all six performance indicators is quite clearer. Advancing combustion in the squish region — characterized by an earlier inflection point — significantly enhances engine performance by reducing COV, increasing BTE, including combustion efficiency improvement. This led to lower methane and CO emissions at the expense of increased heat losses and  $\mathrm{NO}_{\mathrm{x}}$  emissions. The observed peak in heat losses and  $\mathrm{NO}_{\mathrm{x}}$  emissions at the minimum inflection point suggests that most of the fuel is consumed during Phase II, closer to TDC, resulting in elevated in-cylinder temperatures. This explains why COV, methane, and CO emissions reach their lower values under these conditions.

#### 5. Conclusions and recommendations

This study presented a comprehensive experimental investigation of a 500 kWe natural gas lean-burn spark ignition (LBSI) marine engine, uniquely characterizing its dual-phase combustion process (bowl-in and squish combustion) in a marine-scale, multi-cylinder configuration. By integrating insights from recent optical access studies, this work provides new understanding of how fuel distribution and combustion phasing affect overall LBSI engine performance. The major conclusions and recommendations during this research are:

- A clear relationship is found between combustion phasing and engine performance: advancing the inflection point (flame reaching the squish region) consistently improved stability, combustion and thermal efficiency, at the expense of higher heat losses and NO<sub>x</sub> emissions.
- The squish combustion phase is sensitive to operating parameters that advance combustion phasing — particularly spark timing. Spark timing advancement produced opposite trends in two main phases: the bowl-in phase shortened from 26.2 °CA 18 °CA, while the squish phase was prolonged from 12.2 °CA to 16.8 °CA.

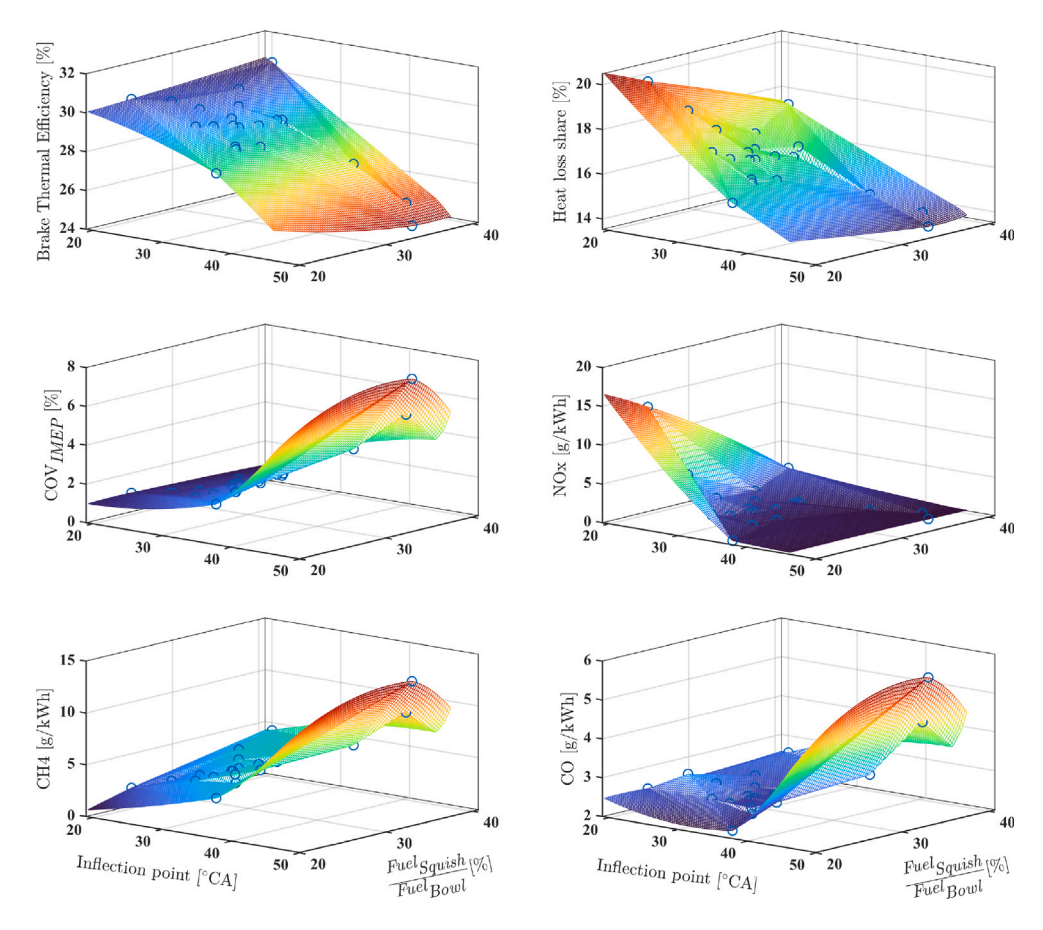


Fig. 21. Relationship between fuel burnt ratio across the two distinguished phases and inflection point with performance indicators including BTE (a), Heat loss share (b), COV<sub>IMEP</sub> (c), NO<sub>x</sub> (d), CH<sub>4</sub> (e), CO (f), across all discrete operating points at 200 kWe.

- Although advanced ignition timing had a diminishing effect on combustion efficiency due to its impact on the squish phase, both mixture enrichment and spark timing advancement sweeps led to improved engine performance, resulting in increases in brake thermal efficiency of 25% and 10%, respectively.
- Methane emissions remained within the expected range for marine SI engines, and  $\mathrm{NO}_{\mathrm{x}}$  emissions were kept within the IMO Tier III limit of 2.08 g/kWh for this engine at nominal conditions. An air excess ratio between 1.45 and 1.60 offered the best compromise between  $\mathrm{NO}_{\mathrm{x}}$  and unburned hydrocarbon emissions, maintaining their sum below 6.5 g/kWh. Nevertheless, the remaining levels and occasional rise of methane emissions under certain operating conditions continue to pose a significant challenge for these engines and future marine engine development. These findings highlight the urgent need for comprehensive regulatory standards that address both  $\mathrm{NO}_{\mathrm{x}}$  and  $\mathrm{CH}_{\mathrm{4}}$  emissions, given methane's significant global warming potential and its current lack of regulation in marine applications.
- Optimization-oriented Design-of-Experiments (DoE) methodologies are recommended to further assess and enhance the performance of this SI engine concept, particularly in optimizing the interaction between air-to-fuel ratio and spark timing for favorable combustion phasing.

These findings provide valuable insights into the unique combustion characteristics of homogeneous open-chamber LBSI concepts that are highly suitable for retrofitting diesel engines. By optimizing critical parameters such as combustion phasing and methane emissions, these engines can play a pivotal role in advancing the energy transition in the marine sector.

# CRediT authorship contribution statement

Konstantinos I. Kiouranakis: Writing – original draft, Visualization, Software, Methodology, Investigation, Formal analysis, Conceptualization. Peter de Vos: Writing – review & editing, Visualization, Supervision, Methodology, Conceptualization. Robbert Willems: Writing – review & editing, Visualization, Methodology, Investigation, Conceptualization. Harsh Darshan Sapra: Writing – review & editing, Methodology, Investigation. Rinze Geertsma: Writing – review & editing, Supervision, Investigation, Funding acquisition.

#### **Declaration of competing interest**

The authors declare the following financial interests/personal relationships which may be considered as potential competing interests: Konstantinos Ioannis Kiouranakis. reports financial support was provided by Netherlands Enterprise Agency. If there are other authors, they declare that they have no known competing financial interests or personal relationships that could have appeared to influence the work reported in this paper.

#### Acknowledgments

Present work is part of the MENENS project (Methanol als Energiestap Naar Emissieloze Nederlandse Scheepvaart). The project is funded by the Netherlands Enterprise Agency (RVO: Rijksdienst voor Ondernemend Nederland) under the grant number MOB21012. Gratitude is extended to the Netherlands Defence Academy (NLDA) engine lab team, especially Marcel Roberscheuten, for their unwavering support.

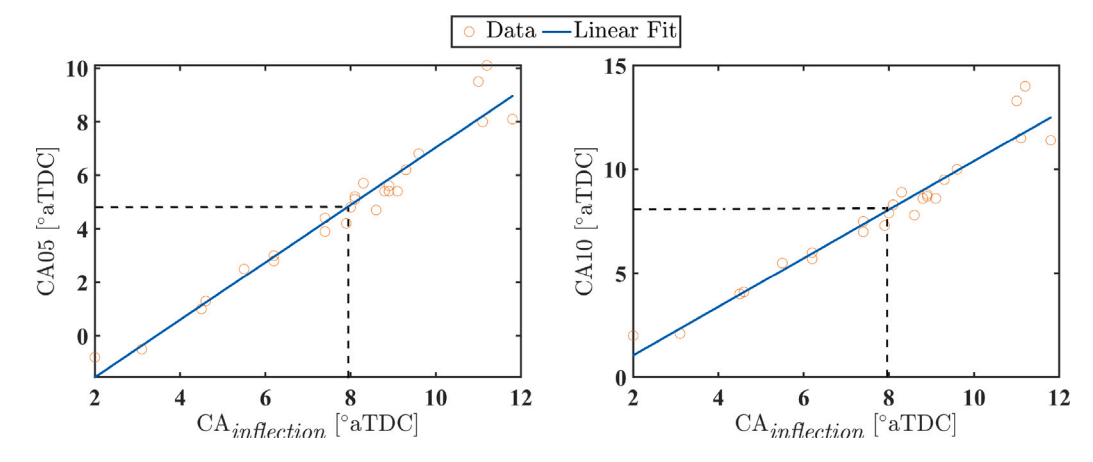


Fig. 22. Correlations between combustion phasing indicators CA05 and CA10 with the first inflection point of aHRR.

Table 8
Heat loss calibrating factors.

Case	Heat loss coefficient $C_0$ [-]						
1	228.9	6	224.7	14	216.3	20	226.8
2	222.6	7	224.7	15	218.4	21	231
3	218.4	8	228.9	16	222.6	22	228.9
4	203.7	9	231	17	228.9	23	228.9
5	193.2	10	233.1	18	231	24	228.9
		11	233.1	19	233.1	25	231
		12	243.6			26	231
		13	249.9				

# Appendix A. Additional information to combustion staging methodology

See Fig. 22.

# Appendix B. Heat transfer calibration factors

See Table 8.

#### Data availability

Data will be made available on request.

#### References

- V. Smil, Numbers don't Lie: 71 Stories to Help Us Understand the Modern World, Penguin Books, [New York, New York], 2021.
- [2] S.K. Mahendar, A. Erlandsson, L. Adlercreutz, Challenges for spark ignition engines in heavy duty application: a review, 2018, http://dx.doi.org/10.4271/ 2018-01-0907, 2018-01-0907.
- [3] C. Mounaïm-Rousselle, P. Bréquigny, C. Dumand, S. Houillé, Operating limits for ammonia fuel spark-ignition engine, Energies 14 (14) (2021) 4141, http://dx.doi.org/10.3390/en14144141.
- [4] S. Verhelst, J.W. Turner, L. Sileghem, J. Vancoillie, Methanol as a fuel for internal combustion engines, Prog. Energy Combust. Sci. 70 (2019) 43–88, http://dx.doi.org/10.1016/j.pecs.2018.10.001.
- [5] B. Shadidi, G. Najafi, T. Yusaf, A review of hydrogen as a fuel in internal combustion engines, Energies 14 (19) (2021) 6209, http://dx.doi.org/10.3390/ en14196209.
- [6] S. Curran, A. Onorati, R. Payri, A.K. Agarwal, C. Arcoumanis, C. Bae, K. Boulouchos, F. Dal Forno Chuahy, M. Gavaises, G.J. Hampson, C. Hasse, B. Kaul, S.-C. Kong, D. Kumar, R. Novella, A. Pesyridis, R. Reitz, B.M. Vaglieco, N. Wermuth, The future of ship engines: Renewable fuels and enabling technologies for decarbonization, Int. J. Engine Res. (2023) 14680874231187954, http://dx.doi.org/10.1177/14680874231187954.
- [7] P.T. Aakko-Saksa, K. Lehtoranta, N. Kuittinen, A. Järvinen, J.-P. Jalkanen, K. Johnson, H. Jung, L. Ntziachristos, S. Gagné, C. Takahashi, P. Karjalainen, T. Rönkkö, H. Timonen, Reduction in greenhouse gas and other emissions from ship engines: Current trends and future options, Prog. Energy Combust. Sci. 94 (2023) 101055, http://dx.doi.org/10.1016/j.pecs.2022.101055.

- [8] K.I. Kiouranakis, P. De Vos, K. Zoumpourlos, A. Coraddu, R. Geertsma, Methanol for heavy-duty internal combustion engines: Review of experimental studies and combustion strategies, Renew. Sustain. Energy Rev. 214 (2025) 115529, http://dx.doi.org/10.1016/j.rser.2025.115529.
- [9] B. Johansson, K. Olsson, Combustion chambers for natural gas SI engines part
   I: Fluid flow and combustion, 1995, 950469, http://dx.doi.org/10.4271/950469,
   URL https://www.sae.org/content/950469/.
- [10] J. Liu, C.E. Dumitrescu, Flame development analysis in a diesel optical engine converted to spark ignition natural gas operation, Appl. Energy 230 (2018) 1205–1217, http://dx.doi.org/10.1016/j.apenergy.2018.09.059.
- [11] M.G.K. Jones, D.M. Heaton, Nebula Combustion System for Lean Burn Spark Ignited Gas Engines, SAE Technical Paper 890211, 1989, http://dx.doi.org/10. 4271/890211.
- [12] R.L. Evans, Lean-burn spark-ignited internal combustion engines, in: Lean Combustion, Elsevier, 2008, pp. 95–120, http://dx.doi.org/10.1016/B978-012370619-5.50005-4, URL https://linkinghub.elsevier.com/retrieve/pii/ B9780123706195500054.
- [13] S.K. Chen, N.J. Beck, Gas engine combustion principles and applications, 2001, http://dx.doi.org/10.4271/2001-01-2489, URL https://www.sae. org/content/2001-01-2489/, pp. 2001-01-2489.
- [14] V. AEsoy, P. Magne Einang, D. Stenersen, E. Hennie, I. Valberg, LNG-fuelled engines and fuel systems for medium-speed engines in maritime applications, 2011, http://dx.doi.org/10.4271/2011-01-1998, URL https://www.sae. org/content/2011-01-1998/, pp. 2011-01-1998.
- [15] T. Humerfelt, E. Johannessen, E. Vaktskjold, L. Skarbö, Development of the rollsroyce c26: 33 marine gas engine series, in: 26th CIMAC World Congress, 2010, pager, no. 54
- [16] K. Olsson, B. Johansson, Combustion chambers for natural gas SI engines part 2: Combustion and emissions, 1995, 950517, http://dx.doi.org/10.4271/950517, URL https://www.sae.org/content/950517/.
- [17] C.D. De Boer, D.W. Grigg, Gasoline Engine Combustion The Nebula Combustion Chamber, SAE Technical Paper 885148, 1988, http://dx.doi.org/10.4271/885148.
- [18] M. Kaplan, Influence of swirl, tumble and squish flows on combustion characteristics and emissions in internal combustion engine-review, Int. J. Automot. Eng. Technol. 8 (2) (2019) 83–102. http://dx.doi.org/10.18245/jijaet.558258.
- [19] J. Liu, C.E. Dumitrescu, Combustion partitioning inside a natural gas spark ignition engine with a bowl-in-piston geometry, Energy Convers. Manage. 183 (2019) 73–83, http://dx.doi.org/10.1016/j.enconman.2018.12.118.
- [20] P. Einewall, B. Johansson, Combustion Chambers for Supercharged Natural Gas Engines, SAE Technical Paper 970221, 1997, http://dx.doi.org/10.4271/970221.
- [21] J. Liu, C.J. Ulishney, C.E. Dumitrescu, Experimental investigation of a heavy-duty natural gas engine performance operated at stoichiometric and lean operations, Energy Convers. Manage. 243 (2021) 114401, http://dx.doi.org/10.1016/j.enconman.2021.114401.

- [22] I. Singh, A. Güdden, A. Raut, A. Dhongde, A. Emran, V. Sharma, S. Wagh, Experimental and numerical investigation of a single-cylinder methanol port-fuel injected spark ignition engine for heavy-duty applications, Pune, India, 2024, http://dx.doi.org/10.4271/2024-26-0072, URL https://www.sae.org/content/2024-26-0072, pp. 2024-26-0072.
- [23] S.K. Mahendar, T. Larsson, A.C. Erlandsson, Alcohol lean burn in heavy duty engines: Achieving 25 bar IMEP with high efficiency in spark ignited operation, Int. J. Engine Res. 22 (11) (2021) 3313–3324, http://dx.doi.org/10.1177/ 1468087420972897.
- [24] A. Sharafian, P. Blomerus, W. Mérida, Natural gas as a ship fuel: Assessment of greenhouse gas and air pollutant reduction potential, Energy Policy 131 (2019) 332–346, http://dx.doi.org/10.1016/j.enpol.2019.05.015.
- [25] E. Fridell, H. Salberg, K. Salo, Measurements of emissions to air from a marine engine fueled by methanol, J. Mar. Sci. Appl. 20 (1) (2021) 138–143, http: //dx.doi.org/10.1007/s11804-020-00150-6.
- [26] P. Lott, O. Deutschmann, Lean-burn natural gas engines: Challenges and concepts for an efficient exhaust gas aftertreatment system, Emiss. Control. Sci. Technol. 7 (1) (2021) 1–6, http://dx.doi.org/10.1007/s40825-020-00176-w.
- [27] J. Liu, C. Ulishney, C. Dumitrescu, Characterization of Cycle-by-Cycle Variations of an Optically Accessible Heavy-Duty Diesel Engine Retrofitted to Natural Gas Spark Ignition, SAE Technical Paper Series, SAE Technical Paper 2021-24-0045, SAE International, 400 Commonwealth Drive, Warrendale, PA, United States, 2021, http://dx.doi.org/10.4271/2021-24-0045, ISSN: 0148-7191.
- [28] P. Corbo, M. Gambino, S. Iannaccone, A. Unich, Comparison between lean-burn and stoichiometric technologies for CNG heavy-duty engines, 1995, 950057, http://dx.doi.org/10.4271/950057, URL https://www.sae.org/content/950057/.
- [29] A. Das, H.C. Watson, Development of a natural gas spark ignition engine for optimum performance, Proc. Inst. Mech. Eng. D: J. Automob. Eng. 211 (5) (1997) 361–378. http://dx.doj.org/10.1243/0954407971526506.
- [30] J. Liu, C.E. Dumitrescu, Limitations of natural gas lean burn spark ignition engines derived from compression ignition engines, J. Energy Resour. Technol. 142 (12) (2020) 122308, http://dx.doi.org/10.1115/1.4047404.
- [31] M. Reyes, F. Tinaut, B. Giménez, A. Pérez, Characterization of cycle-to-cycle variations in a natural gas spark ignition engine, Fuel 140 (2015) 752–761, http://dx.doi.org/10.1016/j.fuel.2014.09.121.
- [32] G.A. Karim, I. Wierzba, Experimental and Analytical Studies of the Lean Operational Limits in Methane Fuelled Spark Ignition and Compression Ignition Engines. SAE Technical Paper 891637, 1989, http://dx.doi.org/10.4271/891637.
- [33] C.E. Dumitrescu, V. Padmanaban, J. Liu, An experimental investigation of early flame development in an optical spark ignition engine fueled with natural gas, J. Eng. Gas Turbines Power 140 (8) (2018) 082802, http://dx.doi.org/10.1115/ 14039616
- [34] J.B. Heywood, Internal Combustion Engine Fundamentals, second ed., McGraw-Hill Education, New York, 2018.
- [35] J. Liu, C.E. Dumitrescu, Analysis of two-stage natural-gas lean combustion inside a diesel geometry, Appl. Therm. Eng. 160 (2019) 114116, http://dx.doi.org/10. 1016/j.applthermaleng.2019.114116.
- [36] J. Liu, C.E. Dumitrescu, Lean-burn characteristics of a heavy-duty diesel engine retrofitted to natural-gas spark ignition, J. Eng. Gas Turbines Power 141 (7) (2019) 071013, http://dx.doi.org/10.1115/1.4042501.
- [37] J. Liu, C.E. Dumitrescu, Methodology to separate the two burn stages of natural-gas lean premixed-combustion inside a diesel geometry, Energy Convers. Manage. 195 (2019) 21–31, http://dx.doi.org/10.1016/j.encomman.2019.04.091.
- [38] C.E.C. Alvarez, G.E. Couto, V.R. Roso, A.B. Thiriet, R.M. Valle, A review of prechamber ignition systems as lean combustion technology for SI engines, Appl. Therm. Eng. 128 (2018) 107–120, http://dx.doi.org/10.1016/j.applthermaleng. 2017.08.118.
- [39] E. Shapiro, N. Tiney, P. Kyrtatos, M. Kotzagianni, M. Bolla, K. Boulouchos, G. Tallu, G. Lucas, M. Weissner, Experimental and numerical analysis of prechamber combustion systems for lean burn gas engines, 2019, http://dx.doi.org/10.4271/2019-01-0260, 2019-01-0260.
- [40] M. Cakir, Effect of stratified charge combustion chamber design on natural gas engine performance, Energies 18 (9) (2025) 2187, http://dx.doi.org/10.3390/ en18092187.
- [41] Y. Tsuji, Y. Kondo, T. Horie, Y. Sakai, Flexible Operation of Gas Engines for Grid Power Stability and Carbon Neutrality, CIMAC, Zurich, 2025.
- [42] N. Peters, M. Bunce, Optimization of Pre-Chamber Design and Operation for Marine Future Fuels, CIMAC, Zurich, 2025.
- [43] L.F. Alvarez, C.E. Dumitrescu, Experimental study of ammonia combustion in a heavy-duty diesel engine converted to spark ignition operation, 2024, http:// dx.doi.org/10.4271/2024-01-2371, URL https://www.sae.org/content/2024-01-2371, pp. 2024-01-2371.
- [44] X. Duan, B. Deng, Y. Liu, S. Zou, J. Liu, R. Feng, An experimental study the impact of the hydrogen enrichment on cycle-to-cycle variations of the large bore and lean burn natural gas spark-ignition engine, Fuel 282 (2020) 118868, http://dx.doi.org/10.1016/j.fuel.2020.118868.
- [45] Y. Li, F. Yang, X. Linxun, J. Liu, J. Wang, X. Duan, Influences of the control parameters and spark plug configurations on the performance of a natural gas spark-ignition engine, Fuel 324 (2022) 124728, http://dx.doi.org/10.1016/j.fuel. 2022.124728.

- [46] Z. Wang, X. Su, X. Wang, D. Jia, D. Wang, J. Li, Impact of ignition energy on the combustion performance of an SI heavy-duty stoichiometric operation natural gas engine, Fuel 313 (2022) 122857, http://dx.doi.org/10.1016/j.fuel.2021.122857.
- [47] P. Sandeep Varma, M. Mittal, Investigations with bowl-in-piston (CI type) and flat-piston (SI type) geometries to study the engine characteristics of a CI engine retrofitted for SI operation with CNG fuel, Energy Convers. Manage. 301 (2024) 118083, http://dx.doi.org/10.1016/j.enconman.2024.118083.
- [48] F. Aktas, Spark ignition timing effects on a converted diesel engine using natural gas: A numerical study, Proc. Inst. Mech. Eng. Part D: J. Automob. Eng. 236 (9) (2022) 1949–1963. http://dx.doi.org/10.1177/09544070221081671.
- [49] L. Danny Harvey, A guide to global warming potentials (GWPs), Energy Policy 21 (1) (1993) 24–34, http://dx.doi.org/10.1016/0301-4215(93)90205-T.
- [50] N. Kuittinen, M. Heikkilä, K. Lehtoranta, Review of Methane Slip from LNG Marine Engines, Technical Report, 2023, URL https://greenray-project.eu/wp-content/uploads/2023/04/D1.1 Review of methane slip from LNG engines.pdf.
- [51] H.D. Sapra, Y. Linden, W. Van Sluijs, M. Godjevac, K. Visser, Experimental Investigations of Hydrogen-Natural Gas Engines for Maritime Applications, American Society of Mechanical Engineers, San Diego, California, USA, 2018, V001T02A004, http://dx.doi.org/10.1115/ICEF2018-9615.
- [52] J. Bosklopper, H. Sapra, R. van de Ketterij, W. van Sluijs, C. Bekdemir, P. de Vos, K. Visser, Experimental study on a retrofitted marine size spark-ignition engine running on portinjected 100% methanol, in: INEC 2020, Delft, 2020.
- [53] D.R. Lancaster, R.B. Krieger, J.H. Lienesch, Measurement and Analysis of Engine Pressure Data, SAE Technical Paper 750026, 1975, http://dx.doi.org/10.4271/ 750026.
- [54] M.F.J. Brunt, C.R. Pond, Evaluation of Techniques for Absolute Cylinder Pressure Correction, SAE Technical Paper 970036, 1997, http://dx.doi.org/10.4271/970036.
- [55] K.I. Kiouranakis, P. De Vos, H. Sapra, R. Geertsma, Natural gas for marine leanburn spark ignition engines: A combustion stability analysis, in: ASME 2024 ICE Forward Conference, American Society of Mechanical Engineers, San Antonio, Texas, USA, 2024, V001T01A002, http://dx.doi.org/10.1115/ICEF2024-139218.
- [56] T.M. Inc., MATLAB version: 23.2.0 (R2023b), 2023, URL https://www.mathworks.com.
- [57] A.L. Randolph, Methods of Processing Cylinder-Pressure Transducer Signals to Maximize Data Accuracy, SAE Technical Paper 900170, 1990, http://dx.doi.org/ 10.4271/900170.
- [58] W. Sun, W. Du, X. Dai, X. Bai, Z. Wu, A Cylinder Pressure Correction Method Based on Calculated Polytropic Exponent, SAE Technical Paper 2017-01-2252, 2017, http://dx.doi.org/10.4271/2017-01-2252.
- [59] M.J. Sta S, Thermodynamic Determination of T.D.C. in Piston Combustion Engines, SAE Technical Paper 960610, 1996, http://dx.doi.org/10.4271/960610.
- [60] M. Tazerout, O. Le Corre, S. Rousseau, TDC determination in IC engines based on the thermodynamic analysis of the temperature-entropy diagram, 1999, http:// dx.doi.org/10.4271/1999-01-1489, URL https://www.sae.org/content/1999-01-1489/, pp. 1999-01-1489.
- [61] F. Payri, J. Luján, J. Martín, A. Abbad, Digital signal processing of in-cylinder pressure for combustion diagnosis of internal combustion engines, Mech. Syst. Signal Process. 24 (6) (2010) 1767–1784, http://dx.doi.org/10.1016/j.ymssp. 2009.12.011.
- [62] R.K. Maurya, Estimation of optimum number of cycles for combustion analysis using measured in-cylinder pressure signal in conventional CI engine, Meas. 94 (2016) 19–25, http://dx.doi.org/10.1016/j.measurement.2016.07.065.
- [63] B. Gainey, J.P. Longtin, B. Lawler, A guide to uncertainty quantification for experimental engine research and heat release analysis, SAE Int. J. Engines 12 (5) (2019) 03–12–05–0033, http://dx.doi.org/10.4271/03-12-05-0033.
- [64] I.M. Organization, MARPOL Annex VI and NTC 2008 with Guidelines for Implementation, International Maritime Organization, 2023, http://dx. doi.org/10.62454/KD664E, URL https://imo-epublications.org/content/books/ 9789280117523.
- [65] D. Stapersma, Diesel engines: A Fundamental Approach to Performance Analysis, Turbocharging, Combustion, Emissions and Heat Transfer: Including Thermodynamical Principles. Vol. 3: Combustion, 2009.
- [66] T. Yusaf, P. Baker, I. Hamawand, M. Noor, Effect of compressed natural gas mixing on the engine performance and emissions, Int. J. Automot. Mech. Eng. 8 (2013) 1416–1429, http://dx.doi.org/10.15282/ijame.8.2013.29.0117.
- [67] H. Cho, K. Lee, J. Lee, J. Yoo, K. Min, Measurements and Modeling of Residual Gas Fraction in SI Engines, SAE Technical Paper 2001-01-1910, 2001, http://dx.doi.org/10.4271/2001-01-1910.
- [68] A. Burcat, B. Ruscic, Chemistry, Third Millenium Ideal Gas and Condensed Phase Thermochemical Database for Combustion (With Update from Active Thermochemical Tables), Technical Report ANL-05/20, 925269, 2005, 925269.
- [69] G. Woschni, A Universally Applicable Equation for the Instantaneous Heat Transfer Coefficient in the Internal Combustion Engine, SAE Technical Paper 670931, 1967, http://dx.doi.org/10.4271/670931.
- [70] Y.G. Guezennec, W. Hamama, Two-Zone Heat Release Analysis of Combustion Data and Calibration of Heat Transfer Correlation in an I. C. Engine, SAE Technical Paper 1999-01-0218, 1999, http://dx.doi.org/10.4271/1999-01-0218.
- [71] Z. Liu, Sankey plot, 2025, URL https://www.mathworks.com/matlabcentral/fileexchange/128679-sankey-plot, MATLAB Central File Exchange, Copyright (c) 2023

- $[72] \ \ IMO, \ International \ maritime \ organization, \ 2024, \ URL \ https://www.imo.org/en.$
- [73] D. Stenersen, O. Thonsta, GHG and NOx Emissions from Gas Fuelled Engines: Mapping, Verification, Reduction Technologies, Technical Report, SIN-TEF Ocean AS, URL https://www.nho.no/siteassets/nox-fondet/rapporter/2018/ methane-slip-from-gas-engines-mainreport-1492296.pdf, ????.
- [74] K.I. Kiouranakis, P. de Vos, H. Sapra, R. Geertsma, Using Multi-Stage Wiebe to Characterize the Combustion of a Marine Natural Gas Lean-Burn SI Engine, CIMAC, 2025, http://dx.doi.org/10.5281/ZENODO.15193328, URL https: //zenodo.org/doi/10.5281/zenodo.15193328.
- [75] J. Liu, C.J. Ulishney, C.E. Dumitrescu, Effect of spark timing on the combustion stages seen in a heavy-duty compression-ignition engine retrofitted to natural gas spark-ignition operation, SAE Int. J. Engines 14 (3) (2021) 03–14–03–0020, http://dx.doi.org/10.4271/03-14-03-0020.
- [76] O. Andersson, Experiment!: Planning, Implementing and Interpreting, John Wiley & Sons, 2012.